

Publications

7-23-2023

Advancing Our Understanding of Martian Proton Aurora through a Coordinated Multi-Model Comparison Campaign

Andrea C. G. Hughes
NASA Goddard Space Flight Center / Howard University

Michael Scott Chaffin
LASP

Edwin J. Mierkiewicz
Embry-Riddle Aeronautical University, mierkiee@erau.edu

Justin Deighan
LASP

Rebecca Jolitz
Laboratory of Atmospheric and Space Physics

See next page for additional authors

Follow this and additional works at: <https://commons.erau.edu/publication>



Part of the [Astrophysics and Astronomy Commons](#)

Scholarly Commons Citation

Andrea C. G. Hughes, Michael Scott Chaffin, Edwin J. Mierkiewicz, et al. Advancing Our Understanding of Martian Proton Aurora through a Coordinated Multi-Model Comparison Campaign. ESS Open Archive. July 23, 2023.

This Article is brought to you for free and open access by Scholarly Commons. It has been accepted for inclusion in Publications by an authorized administrator of Scholarly Commons. For more information, please contact commons@erau.edu.

Authors

Andrea C. G. Hughes, Michael Scott Chaffin, Edwin J. Mierkiewicz, Justin Deighan, Rebecca Jolitz, Esa Kallio, Guillaume Gronof, Valery I. Shematovich, Dmitry Bisikalo, Cyril L. Simon Wedlund, Jasper S. Halekas, Nicholas M. Schneider, Birgit Ritter, Zachary Girazian, Sonal Jain, Jean-Claude M. C. Gérard, and Bradley Michael Hegyi

Advancing Our Understanding of Martian Proton Aurora through a Coordinated Multi-Model Comparison Campaign

Andrea C. G. Hughes¹, Michael Scott Chaffin², Edwin J. Mierkiewicz³, Justin Deighan², Rebecca Jolitz⁴, Esa Kallio⁵, Guillaume Gronoff⁶, Valery I. Shematovich⁷, Dmitry Bisikalo⁷, Cyril L. Simon Wedlund⁸, Jasper S. Halekas⁹, Nicholas M. Schneider¹⁰, Birgit Ritter¹¹, Zachary Girazian¹², Sonal Jain², Jean-Claude M. C. Gérard¹³, and Bradley Michael Hegyi¹⁴

¹NASA Goddard Space Flight Center / Howard University

²LASP

³Embry-Riddle Aeronautical University

⁴Laboratory of Atmospheric and Space Physics

⁵Aalto University, School of Electrical Engineering

⁶Nasa Langley Research Center

⁷Institute of Astronomy of the Russian Academy of Sciences

⁸Space Research Institute, OEAW

⁹University of Iowa

¹⁰University of Colorado Boulder

¹¹Royal Observatory of Belgium

¹²The University of Iowa

¹³Université de Liège

¹⁴NASA Langley Research Center

July 23, 2023

Abstract

Proton aurora are the most commonly observed yet least studied type of aurora at Mars. In order to better understand the physics and driving processes of Martian proton aurora, we undertake a multi-model comparison campaign. We compare results from four different proton/hydrogen precipitation models with unique abilities to represent Martian proton aurora: Jolitz model (3-D Monte Carlo), Kallio model (3-D Monte Carlo), Bisikalo/Shematovich et al. model (1-D kinetic Monte Carlo), and Gronoff et al. model (1-D kinetic). This campaign is divided into two steps: an inter-model comparison and a data-model comparison. The inter-model comparison entails modeling five different representative cases using similar constraints in order to better understand the capabilities and limitations of each of the models. Through this step we find that the two primary variables affecting proton aurora are the incident solar wind particle flux and velocity. In the data-model comparison, we assess the robustness of each model based on its ability to reproduce a MAVEN/IUVS proton aurora observation. All models are able to effectively simulate the data. Variations in modeled intensity and peak altitude can be attributed to differences in model capabilities/solving techniques and input assumptions (e.g., cross sections, 3-D versus 1-D solvers, and implementation of the relevant physics and processes). The good match between the observations and multiple models gives a measure of confidence that the appropriate physical processes and their associated parameters have been correctly identified, and provides insight into the key physics that should be incorporated in future models.

1 **Advancing Our Understanding of Martian Proton Aurora through a**
2 **Coordinated Multi-Model Comparison Campaign**
3

4 **Andréa C. G. Hughes^{1,2,3}, Michael Chaffin⁴, Edwin Mierkiewicz³, Justin Deighan⁴, Rebecca**
5 **D. Jolitz⁴, Esa Kallio⁵, Guillaume Gronoff^{6,7}, Valery Shematovich⁸, Dmitry Bisikalo^{8,9},**
6 **Jasper Halekas¹⁰, Cyril Simon Wedlund¹¹, Nicholas Schneider⁴, Birgit Ritter^{12,13}, Zachary**
7 **Girazian¹⁰, Sonal Jain⁴, Jean-Claude Gérard¹², and Bradley Hegyi^{6,7}**

8 ¹ NASA Goddard Space Flight Center, Greenbelt, MD, United States.

9 ² Department of Physics & Astronomy, Howard University, Washington, DC, United States.

10 ³ Center for Space and Atmospheric Research (CSAR) and the Department of Physical Sciences,
11 Embry-Riddle Aeronautical University, Daytona Beach, Florida, United States.

12 ⁴ Laboratory for Atmospheric and Space Physics, University of Colorado, Boulder, CO, USA.
13 United States.

14 ⁵ Aalto University, School of Electrical Engineering, Department of Electronics and
15 Nanoengineering, Espoo, Finland.

16 ⁶ NASA Langley Research Center, Hampton, VA, United States.

17 ⁷ Science Systems and Application Inc. Hampton, VA, United States.

18 ⁸ Institute of Astronomy of the Russian Academy of Sciences, Moscow, Russia.

19 ⁹ National Center for Physics and Mathematics, Russian Federation, Moscow, Russia.

20 ¹⁰ Department of Physics and Astronomy, University of Iowa, Iowa City, IA, United States.

21 ¹¹ Space Research Institute, Austrian Academy of Sciences, Graz, Austria.

22 ¹² Royal Observatory of Belgium, Brussels, Belgium.

23 ¹³ Université de Liège, LPAP – STAR Institute, Liege, Belgium.

24
25 Corresponding author (first): Andrea Hughes (Andrea.C.Hughes@NASA.gov)

26 Corresponding author (second): Michael Chaffin (Michael.Chaffin@colorado.edu)
27

28 **Key Points:**

- 29 ● We undertake a multi-model comparison campaign to gain a better understanding of the
30 physics and driving processes of Martian proton aurora
31 ● The incident solar wind particle flux and velocity are found to be the two most influential
32 parameters affecting the proton aurora profile

- 33 • The models effectively reproduce observations, with variations due to different model
34 capabilities/solving techniques and input assumptions

35

36 **Abstract**

37 Proton aurora are the most commonly observed yet least studied type of aurora at Mars. In
38 order to better understand the physics and driving processes of Martian proton aurora, we
39 undertake a multi-model comparison campaign. We compare results from four different
40 proton/hydrogen precipitation models with unique abilities to represent Martian proton aurora:
41 Jolitz model (3-D Monte Carlo), Kallio model (3-D Monte Carlo), Bisikalo/Shematovich *et al.*
42 model (1-D kinetic Monte Carlo), and Gronoff *et al.* model (1-D kinetic). This campaign is
43 divided into two steps: an inter-model comparison and a data-model comparison. The inter-
44 model comparison entails modeling five different representative cases using similar constraints
45 in order to better understand the capabilities and limitations of each of the models. Through this
46 step we find that the two primary variables affecting proton aurora are the incident solar wind
47 particle flux and velocity. In the data-model comparison, we assess the robustness of each model
48 based on its ability to reproduce a MAVEN/IUVS proton aurora observation. All models are able
49 to effectively simulate the data. Variations in modeled intensity and peak altitude can be
50 attributed to differences in model capabilities/solving techniques and input assumptions (*e.g.*,
51 cross sections, 3-D versus 1-D solvers, and implementation of the relevant physics and
52 processes). The good match between the observations and multiple models gives a measure of
53 confidence that the appropriate physical processes and their associated parameters have been
54 correctly identified, and provides insight into the key physics that should be incorporated in
55 future models.

56

57 Plain Language Summary

58 The purpose of the present study is to gain a deeper understanding of the physics and
59 driving processes of Martian proton aurora through a comparative modeling campaign. The
60 models involved in this study have important similarities and differences, such as the
61 dimensionality (*e.g.*, 3-D versus 1-D), inputs, and relevant physics included. We separate the
62 modeling campaign into two steps: a first step comparing the models with each other (*i.e.*,
63 model-model comparison), and a second step comparing the simulated model results with data
64 from a proton aurora observation (*i.e.*, data-model comparison) taken by the Imaging UltraViolet
65 Spectrograph (IUVS) onboard the Mars Atmosphere and Volatile Evolution (MAVEN)
66 spacecraft. We find that all of the models are able to effectively simulate the data in terms of
67 shape and brightness range of the proton aurora observation. The results of this study inform our
68 understanding of the primary influencing factors that cause variability in the Martian proton
69 aurora profile, the effects of dynamically changing solar wind parameters on the coupled Mars-
70 Sun auroral system (*e.g.*, through extreme solar events such as coronal mass ejections and solar
71 wind stream interactions), and the physical processes/constraints that should be considered in
72 future modeling attempts of this unique phenomenon.

73

74 1. Introduction and Background

75 Proton aurora have been recently determined to be the most commonly observed type of
76 aurora at Mars (Hughes *et al.*, 2019). This form of aurora is one of three primary types of
77 Martian aurora, in addition to discrete (Bertaux *et al.*, 2005) and diffuse aurora (Schneider *et al.*,
78 2015). Further, even though this phenomenon was theoretically predicted by Kallio and Barabash
79 (2001), proton aurora is the most recently discovered type of Martian aurora (Deighan *et al.*,
80 2018; Ritter *et al.*, 2018), and is thereby arguably one of the least studied and understood types
81 of Martian aurora. Past efforts to model these phenomena have been unable to fully reproduce
82 the observations (*e.g.*, Deighan *et al.*, 2018, in which the shape of the modeled profile resembled
83 the data, but the modeled peak altitudes were consistently below the data and modeled intensities
84 required adjustment via a scaling factor to match the data), suggesting a gap in our understanding
85 and a need for further exploration of the underlying physics of these events through modeling.

86 Proton aurora can be identified in ultraviolet data as an enhancement in the hydrogen (H)
87 Lyman-alpha ($\text{Ly-}\alpha$) emission (121.6 nm) above the background coronal H brightness between
88 an altitude of ~ 110 -150 km; this enhancement is due to the contribution from the proton aurora-
89 inducing H energetic neutral atoms (ENAs) as they collide with the atmosphere and emit photons
90 (see Figure 1 from Hughes *et al.*, 2019 for more detail and explanation of formation processes).
91 In a previous statistical study, Hughes *et al.* (2019) used multiple Mars years of data from the
92 Imaging UltraViolet Spectrograph (IUVS) (McClintock *et al.*, 2015) onboard the Mars
93 Atmosphere and Volatile EvolutioN (MAVEN) spacecraft (Jakosky *et al.*, 2015) to assess the
94 phenomenology of Martian proton aurora. Based on this study, they found that most Martian
95 proton aurora events occur on the dayside of the planet (*i.e.*, at low solar zenith angles, SZAs)
96 around the southern summer solstice (*i.e.*, solar longitude, L_s , $\sim 270^\circ$). This seasonal increase in
97 proton aurora activity was found to be correlated with the inflated Martian H corona around
98 southern summer solstice, which corresponds with higher H column densities and H escape rates,
99 caused by upper atmospheric temperatures and dust activity reaching an annual maximum during
100 this time (*e.g.*, Hughes *et al.*, 2019; Chaffin *et al.*, 2021; Chaffin *et al.*, 2014; Clarke *et al.*, 2014;
101 Halekas, 2017). This annual variability is also coupled with slightly higher solar wind proton
102 fluxes as Mars is near perihelion ($L_s = 251^\circ$). The seasonally increased abundance of H beyond
103 the planet's bow shock during this season allows a larger fraction of solar wind protons to be
104 converted into hydrogen ENAs (H-ENAs) (*i.e.*, through charge exchange), which can then
105 bypass the bow shock and magnetic pileup boundary to create more frequent proton aurora
106 events with very large $\text{Ly-}\alpha$ emission enhancements during this time of year.

107 The purpose of the present study is to gain a deeper understanding of the physics and
108 driving processes of Martian proton aurora through a comparative modeling campaign. While
109 previous data-driven statistical studies of these aurora provided an understanding of their
110 phenomenology, frequency, and likely driving processes, much is still lacking in our knowledge.
111 This includes, for example, the specific effects of variability in different input parameters on the
112 shape, brightness, and peak altitude of the proton aurora profile, as well as the influence of
113 model capabilities, solving techniques, and input assumptions on effectively simulating proton
114 aurora observations. Modeling proton aurora activity provides an opportunity to understand these
115 events, as it allows us to constrain different input parameters and predict variations in the results.
116 Moreover, by undertaking a comparative modeling campaign in which the results of multiple
117 models are evaluated (with each model emphasizing specific physical processes and utilizing
118 different numerical solving techniques), we are able to simultaneously explore the range of

119 possible outcomes for individual auroral events. We note that the statistical study by Hughes *et*
120 *al.* (2019) incorporated data from only the first ~two Mars years of MAVEN orbits, taken during
121 the declining and minimum portion of the solar cycle. While the Hughes *et al.* (2019) study
122 encompassed many proton aurora events, in this study we focus our efforts on modeling one
123 specific event from the IUVS dataset that exhibited particularly interesting proton aurora
124 activity.

125 Being able to effectively model Martian proton aurora is necessary for developing our
126 understanding of observations of auroral events in the IUVS dataset, as well as the ability to
127 predict and understand future observations. The purpose of this modeling campaign is not to
128 determine which model is the “best” proton/hydrogen precipitation model in our study, but rather
129 to identify the distinct capabilities each model provides in simulating proton/hydrogen
130 precipitation at Mars. Through undertaking a rigorous assessment of Martian proton aurora using
131 the results of multiple different simulations, we are able to develop an understanding of the gaps
132 in our knowledge and improve our abilities to more effectively model future proton aurora
133 observations.

134 2. Modeling Campaign Description

135 2.1. Campaign Outline/Steps

136 In order to accomplish the goals of this study, this campaign is divided into two primary
137 steps: an inter-model comparison step (Step 1) and a data-model comparison step (Step 2). Each
138 step is subdivided to reflect the “native format” (*i.e.*, original model outputs) and “forward-
139 modeled” (*i.e.*, after running model outputs through radiative transfer model – described in more
140 detail below) results (*i.e.*, Steps 1-A and 1-B, as well as Steps 2-A and 2-B). In the following
141 sections we describe the models and discuss the results of each of these steps. We also consider
142 the assumptions of each model and compare differences in the model capabilities (*e.g.*, the
143 physics represented in each model) that may impact the results.

144 2.2. Models and Modeling Teams Involved in Campaign

145 In this study we utilize four different proton/hydrogen precipitation models and one
146 radiative transfer model. Here we briefly discuss the different models and teams involved.
147 Detailed descriptions of each of the four proton/hydrogen precipitation models used in the study
148 and an overview table comparing their cross section assumptions are provided in supplementary
149 material (Text S1-S4 and Table S1). A radiative transfer (RT) model is then used to “forward-
150 model” the results of each step into observation space (*i.e.*, Steps 1-B and 2-B, respectively); this
151 model is also briefly described below.

152 2.2.1. Proton/Hydrogen Precipitation Models

153 We include four unique proton/hydrogen precipitation models in this study: the Jolitz
154 model (*i.e.*, “ASPEN”), the Kallio model, the Bisikalo/Shematovich *et al.* model, and the
155 Gronoff *et al.* model (*i.e.*, “Aeroplanets”). The former three are Monte Carlo (MC) models (with
156 the Jolitz and Kallio models being 3-dimensional (3-D) and the Bisikalo/Shematovich *et al.*
157 model being 1-D). A MC simulation is a numerical technique that generates a range of possible
158 outcomes and probabilities of occurrence for specific representative inputs. In such a simulation,
159 a mathematical model is first constructed and then iteratively run using different random input

160 variables; the results can be considered in the context of a probability distribution curve and are
161 averaged together to estimate the most likely outcome. In contrast, the Gronoff *et al.* model uses
162 a 1-D Kinetic scheme, based on a semi-analytical treatment of the coupled H⁺/H Boltzmann
163 kinetic transport equation.

164 2.2.1.1. *Jolitz 3-D Monte Carlo model (“ASPEN”)*

165 The Jolitz model, *i.e.*, ASPEN (Atmospheric Scattering of Protons, Electrons, and
166 Neutrals), is a 3-D Monte Carlo test particle simulation. This model was initially developed to
167 predict atmospheric ionization rates at Mars by solar energetic particles, which have higher
168 energies than the ENAs studied in this paper (Jolitz *et al.*, 2017), and has since been used to
169 predict precipitating SEP electron fluxes at Mars (Jolitz *et al.*, 2021). The model solves the
170 Lorentz force equations for energetic particle motion and uses a Monte Carlo approach to predict
171 collisions and resulting energy loss in the atmosphere.

172 Using ASPEN, stochastic collisions are modeled by inverting the relation between
173 intensity, density, and absorption cross section for a particle beam incident on a medium of
174 scatterers (colloquially known as Beer’s law) to dynamically calculate a probability distribution
175 function that is combined with a random number to predict variable distances between collisions.
176 This probability distribution function is calculated for each individual particle and depends on
177 the position, path, and energy through the planetary atmosphere. Similarly, whenever a collision
178 occurs, the type of collision is predicted probabilistically using the relative cross section of each
179 possible collisional process and the particle energy is decremented by the corresponding energy
180 loss. As a particle loses energy, the relative cross sections of each process change.

181 This model (as well as all models in this study) is highly dependent on the choice of cross
182 sections. For the application in this study, the selected cross sections for hydrogen and proton
183 impact on carbon dioxide are described in Jolitz *et al.* (2017), with one exception: the cross
184 sections for proton- and hydrogen-impact excitation was replaced with Ly- α emission cross
185 sections. ASPEN uses a cross section calculated by scaling the corresponding emission cross
186 sections from impact on molecular oxygen.

187 Since ASPEN is a 3-D Monte Carlo simulation, predicting an accurate emission rate
188 requires appropriate choice of initial conditions and a large volume of simulated particles. For
189 Step 1, we simulate 10,000 particles incident on the subsolar point from an altitude of 600 km
190 and calculated the emission rate by binning all Ly- α emitting collisions as a function of altitude
191 and multiplying by the incident flux. For Step 2, we simulate 10,000 particles uniformly
192 distributed in space on a plane perpendicular to the direction of solar wind flow. Each particle
193 represents a fraction of the assumed incident flux. The emission rate was then calculated by
194 weighing the total number of emissions binned by altitude, solar zenith angle, and the fraction of
195 flux associated with each simulated particle.

196 2.2.1.2. *Kallio 3-D Monte Carlo model*

197 The Kallio model is a 3-D Monte Carlo model where the incident particle, either H⁺ or H,
198 collides with neutral particles, after which the velocity of the particle is changed. The model
199 includes 6 elastic and 24 inelastic processes; however, in this study, only the processes
200 mentioned in the main text of this paper were used.

201 The model inputs are neutral atom densities, energy dependent total cross sections, the
202 differential scattering cross sections (DSCS), the number of precipitating particles (5,000
203 particles in the Step 1 runs and 100,000 particles in Step 2 runs), and the initial positions and
204 velocities of the precipitating particles (in the present case hydrogen atoms). The total cross
205 sections are given in Kallio and Barabash (2001, Table 1 and Fig. 3) and the DSCS scattering
206 angle distribution in Kallio and Barabash (2000, Fig. 1, “nominal”) and Kallio and Barabash
207 (2001, Fig. 2). Total cross sections give the probability that a collision occurs. Random numbers
208 are used to model if a collision occurs, and which collision process occurs. If a collision happens,
209 then the DSCS determines the new velocity of the incident particle after collision. The value of
210 the scattering angle is obtained by using a new random variable.

211 The largest uncertainty for the obtained Ly- α volume emission rate is related to the
212 uncertainty of the total cross sections used and the DSCS between H and H⁺ particles and CO₂
213 molecules. In the simulation many of these H/H⁺ collisions with CO₂ are modeled with H/H⁺
214 collisions with O₂ and N₂ which was published in the literature (see Kallio and Barabash, 2001,
215 Table 1, for details).

216 In the simulation, particles are injected into the upper atmosphere at the point $[x, y, z] =$
217 $[260 \text{ km} + R_{\text{Mars}}, 0, 0]$, where the radius of Mars, R_{Mars} , is 3393 km. The model saves the position
218 and the velocity of the particle if it has a Ly- α collision process. The Ly- α volume production
219 rate was derived from the saved positions of Ly- α processes by collecting the number of the Ly-
220 α collision processes at a given altitude range. Then the Ly- α volume emission was derived by
221 using a 1-D approximation, *i.e.*, assuming that the area of the emission perpendicular to the x-
222 axis is equal to the initial area in the solar wind through which the precipitating particles initially
223 came. In the plots presented in this paper the Ly- α emission altitude profiles were derived in 1
224 km altitude bins.

225 2.2.1.3. *Bisikalo/Shematovich et al. 1-D Monte Carlo model*

226 The Bisikalo/Shematovich *et al.* model is a 1-D Monte Carlo model. The model considers
227 three primary processes: 1) precipitation of high-energy hydrogen atoms and protons that lose
228 their kinetic energy in the elastic and inelastic collisions, 2) ionization of target atmospheric
229 molecules/atoms, and 3) charge transfer and electron capture collisions with the major
230 atmospheric constituents (*i.e.*, CO₂, N₂, and O). Secondary fast hydrogen atoms and protons carry
231 enough kinetic energy to cycle through the collisional channels mentioned above and result in a
232 growing set of translationally and internally excited atmospheric atoms and/or molecules.

233 To study the precipitation of high-energy H/H⁺ flux into the planetary atmosphere, we use
234 the kinetic Monte Carlo model to solve the kinetic Boltzmann equations (Shematovich *et al.*,
235 2011; Gérard *et al.*, 2000) for H⁺ and H. The model is 1-D in geometric space and 3-D in
236 velocity space. Nevertheless, the 3-D trajectories of H/H⁺ are calculated in the code with final
237 projection on radial direction. The current version of the MC model (Shematovich *et al.*, 2019)
238 incorporates the full structure of the induced magnetic field of Mars; that is, all three components
239 of the magnetic field $\mathbf{B} = \{B_x, B_y, B_z\}$ are taken into account. The details of the model
240 implementation and statistics control with the variance below 10% can be found in Shematovich
241 *et al.* (2019).

242 The essence of the kinetic Monte Carlo model is accounting of all possible collisions in
243 the atmospheric region studied. Therefore, statistics for all collisional processes are accumulated

244 during the numerical realization of the kinetic model of the proton aurora. It provides a good
245 basis for the evaluation of the Ly- α source functions as keeping all excitation processes and their
246 spatial characteristics makes it possible to determine the statistical distribution of the emitted Ly-
247 α photons.

248 A key aspect of this model is the probabilistic treatment of the scattering angle distribution,
249 which influences both the energy degradation rate and the angular redistribution of the
250 precipitating protons and hydrogen atoms (Bisikalo *et al.*, 2018; Shematovich *et al.*, 2019). The
251 model utilizes both total and differential cross sections when calculating the post-collision
252 velocities for high-energy precipitating H/H⁺ and atmospheric particles.

253 The region under study is limited by the lower boundary, which is placed at 80 km, where
254 H/H⁺ particles are efficiently thermalized. The upper boundary is set at 500 km, where
255 measurements or calculations of the precipitating fluxes of protons or hydrogen atoms are used
256 as a boundary condition. Both table and/or analytic (Maxwellian and/or kappa-distribution)
257 functions representing the energy spectra as well as the pitch-angle (monodirectional, isotropic,
258 or limited by cone) distributions of precipitating particles could be used at the upper boundary.

259 2.2.1.4. Gronoff *et al.* 1-D Kinetic model (“Aeroplanets”)

260 The Gronoff *et al.* model, called Aeroplanets, utilizes a 1-D Kinetic transport approach.
261 Aeroplanets (Gronoff *et al.*, 2012a; Gronoff *et al.*, 2012b; Simon Wedlund *et al.*, 2011) is based
262 on an auroral particle precipitation model initially developed for the Earth and later adapted to
263 Mars (as well as numerous other planetary bodies, *e.g.*, Venus and Titan). This model computes
264 the ionization and excitation of atmospheric species by photon, electron, proton, and cosmic ray
265 impacts, including the effect of secondary particles. The proton transport module within
266 Aeroplanets is based on the work of Galand *et al.* (1997 and 1998), Simon (2006), and Simon *et al.*
267 (2007) for Earth, who solved semi-analytically the coupled proton-hydrogen dissipative
268 kinetic transport equation for protons and hydrogen atoms charge-changing with neutral gas. It
269 was originally developed from the idea that dissipative forces responsible for angular
270 redistributions (due to elastic scattering) can be introduced in the force term of the general
271 dissipative Boltzmann equation (Galand *et al.*, 1997). As such, angular redistributions due to
272 magnetic mirroring effects and to collisions are naturally included, leading to backscattering.

273 Inputs to the Aeroplanets model include cross sections, the vertical profile of atmospheric
274 neutral densities (*i.e.*, composition at different altitudes), and the precipitating fluxes of particles
275 such as H and H⁺ at the top of the atmosphere (any shape and energy distribution can be
276 prescribed). Outputs include the vertical profile of H and H⁺ differential energy fluxes, and the
277 vertical profile of the production rate of excited and ionized species and electrons, including
278 emissions. Simulations are performed on a grid typically spanning 90 to 250 km (approximately,
279 the exobase level).

280 Cross sections in Aeroplanets are taken from the latest version of the ATMOCIAD
281 (Gronoff *et al.*, 2021) cross section and reaction rate database compiled and developed by Simon
282 Wedlund *et al.* (2011) and Gronoff *et al.* (2012a). In ATMOCIAD, experimental and theoretical
283 cross sections as well as their uncertainties are collected. Although ATMOCIAD is an extensive
284 collection of cross sections, we note that there is still a rather poor characterization of cross
285 sections at low energies (typically in the sub-keV range). Regarding differential cross sections,
286 Aeroplanets uses phase functions that are convolved with the energy-dependent cross sections
287 described above.

288 Aeroplanets is well qualified for the fast computation of the proton precipitation from a
289 measured spectra near the planet, and for the fast computation of the whole effect of that
290 precipitation thanks to its coupling with a secondary electron transport model. The analytic
291 computation approach prevents the computation within very complex magnetic topologies
292 (which are best handled by Monte-Carlo models) but is suited for handling large sets of initial
293 angles and energies.

294 2.2.2. Radiative Transfer Model

295 To quantitatively compare the proton aurora modeling results and the IUVS limb
296 observations it is necessary to perform a radiative transport calculation (done in this study using
297 a Radiative Transfer model created by coauthor Deighan). While the Ly- α emission from thermal
298 hydrogen is optically thick in the upper atmosphere of Mars (Anderson and Hord, 1971), the
299 emission associated with proton aurora can be considered optically thin due the large Doppler
300 shifting caused by the high velocity of the ENAs (Gérard et al., 2019). This both offsets the line
301 center and broadens the width of the spectral line shape and ensures that few of the photons
302 produced by proton aurora interact with the ambient thermal hydrogen population for most
303 viewing geometries. This allows a simple line-of-sight integration to be employed, though CO₂
304 absorption must still be taken into account (Deighan *et al.*, 2018; Gérard *et al.*, 2019).

305 The procedure used to calculate a model brightness to compare with each measurement
306 by IUVS is as follows: First, the model atmosphere is sampled at 1 km intervals starting from the
307 reconstructed spacecraft position and extending out 3000 km along the line-of-sight vector. This
308 ensures adequate sampling of the model volume emission rate (VER), as the auroral emission
309 typically has a scale height on the order of 10 km and a peak VER occurring 500-1700 km away
310 from the spacecraft for IUVS periapsis limb scans. The column of CO₂ between the spacecraft
311 and each sample point in the model is then integrated and an absorption optical depth is
312 obtained using an absorption cross section of 7.348×10^{-20} cm² (Huestis and Berkowitz, 2010).
313 The Beer-Lambert law is then applied to find the attenuation caused by CO₂ absorption for each
314 sample point and the attenuated VER is integrated to obtain a column emission rate (CER). This
315 is readily converted into the brightness unit of Rayleighs (R) conventionally used for airglow and
316 aurora (Hunten *et al.*, 1956). The proton aurora VER and CO₂ densities are both assumed to have
317 spherical symmetry (primarily driven by the use of 1-D profiles), and the brightness calculation
318 itself is performed using an integration through 3-D space along each line of sight.

319 3. Inputs and Results for Inter-model Comparison (Step 1)

320 3.1. Purpose and Description of Step 1

321 We begin the campaign with an inter-model comparison in Step 1 using multiple
322 different test cases of representative inputs to represent varying proton aurora conditions. The
323 purpose of this step is to set a baseline for inter-model comparisons, and to compare the effects
324 of varying input conditions on the results of each individual model.

325 We use five different representative proton aurora conditions, each with varying solar
326 wind velocity, H-ENA and proton fluxes at the top of the atmosphere, and CO₂ density profiles
327 for high and low atmospheric temperature conditions (Table 1). Using these inputs, altitude
328 versus Ly- α volume emission rate profiles were created by each model for each representative
329 test case. In Step 1-A, we first compare the results in each modeler's native format (*e.g.*, volume

330 emission rate). In Step 1-B the results are forward-modeled into observation space using the
331 radiative transfer model. In Section 5 we discuss possible causes for the observed inter-model
332 discrepancies.

333 3.2. Assumptions/Constraints for Step 1

334 To accurately compare the driving physics incorporated in each of the models, we
335 implement a number of constraints on each model in Step 1 (*i.e.*, the inter-model comparison
336 step). The three primary constraints are 1) assuming the incident solar wind particle beam (either
337 purely H or purely H⁺) is monoenergetic; 2) assuming purely 1-D anti-sunward solar wind
338 particle movement (*i.e.*, monodirectional) incident at the subsolar point (*i.e.*, SZA = 0°); and 3)
339 requiring that the same cross section processes be included in each model (yet allowing the use
340 of different cross section values; see Section 5.1 and Supplementary Table S1 for more details).
341 We empirically justify inclusion of the first two constraints based on previous observations of
342 penetrating protons showing a monoenergetic population (*i.e.*, typically the same energy as the
343 solar wind) that is incident across the entire sunward-facing side of the planet (*e.g.*, Halekas *et al.*,
344 2015). For the third constraint, we specifically consider five cross section processes for
345 protons and/or H interacting with CO₂: elastic, charge exchange/electron capture, electron
346 stripping, ionization, and Ly- α . Although all models have the ability to incorporate additional
347 processes (see Supplementary Table S1), most have incorporated exclusively these five
348 processes. We note that the Bisikalo/Shematovich *et al.* team also included cross section
349 processes for Hydrogen Balmer-alpha and -beta; however, this inclusion produces only a very
350 minor effect on the resulting volume emission rate (VER) due to the relatively small cross
351 sections of these processes. Each modeling team also incorporated their own DSCS values
352 (Supplementary Table S1). Lastly, while the Jolitz and Kallio models use similar 1 km linear
353 altitude bins, the other two models utilize different types of altitude binning (we note however,
354 that a comparison of the type and spatial resolution of the altitude bins used by the Gronoff *et al.*
355 model found that this parameter to have a negligible effect on the simulation results).

356 3.3. Representative inputs for Step 1

357 In undertaking the inter-model comparison, we create five representative proton aurora
358 events to be simulated by each model (Table 1). We select baseline cases that resemble previous
359 observations of the particle flux, velocity, and neutral CO₂ temperature of Martian proton aurora
360 (*e.g.*, Deighan *et al.*, 2018), and incrementally change the input parameters in each case in order
361 to quantify the effect of the parameters on the proton aurora profile. In the two baseline cases we
362 vary the type of incident particle at the top of the model atmosphere (*i.e.*, 100% H-ENAs or
363 100% protons in Case 1 and Case 2, respectively); in subsequent cases we vary the average
364 incident particle beam flux (Case 3), the particle velocity (Case 4), and the neutral atmospheric
365 temperature (Case 5). By changing the temperature in Case 5, we also modify the scale height,
366 and thereby the CO₂ density profile. In Step 1 we do not include any representative cases that
367 consider variability associated with magnetic fields or solar zenith angles (SZAs) (*i.e.*, the
368 models simulate particle incidence at the subsolar point, where the Ly- α intensities are highest on
369 the planet). While these constraints are not necessarily indicative of the actual Mars-solar wind
370 interactions, they represent simplified scenarios that are beneficial for gauging inter-model
371 variability. We note that in this study we are exclusively interested in modeling the proton aurora
372 profile under different input conditions; since proton aurora are almost entirely formed due to
373 interactions between the incident particles and the neutral CO₂ atmosphere, the model results do

374 not directly incorporate processes occurring in the extended corona upstream of the bow shock
 375 (e.g., charge exchange between solar wind protons and the H corona; however, all but Case 2
 376 implicitly include this process).

377 *Table 1: Representative input for the five example cases in the inter-model comparison step (Step 1). These parameters were*
 378 *varied to assess their relative importance in each model.*

	Case 1 (Baseline w/ H-ENAs)	Case 2 (Baseline w/ Protons)	Case 3 (Small Flux)	Case 4 (High Velocity)	Case 5 (Hot Atmosphere)
v [km/s]	400	400	400	800	400
$F_{\text{H-ENA}}$ [$\text{cm}^{-2}\text{s}^{-1}$]	10^7	0	10^6	10^7	10^7
F_{proton} [$\text{cm}^{-2}\text{s}^{-1}$]	0	10^7	0	0	0
CO ₂ Density Profile (varying Temp)	CO ₂ profile @ T=190K	CO ₂ profile @ T=190K	CO ₂ profile @ T=190K	CO ₂ profile @ T=190K	CO ₂ profile @ T=240K

379

380 In order to vary the neutral atmospheric temperature parameter in the models (Case 5) we
 381 create two different CO₂ density profiles, each containing altitude-binned (1 km bin)
 382 representative CO₂ number density values for the two respective temperature ranges of 190 K
 383 (i.e., baseline temperature) and 240 K (i.e., high temperature). These different CO₂ density
 384 values were created using a standard barometric isothermal atmosphere described by the
 385 equation:

386

$$n(z) = n_{\text{ref}} \exp(- (z - z_{\text{ref}}) / H), \quad (1)$$

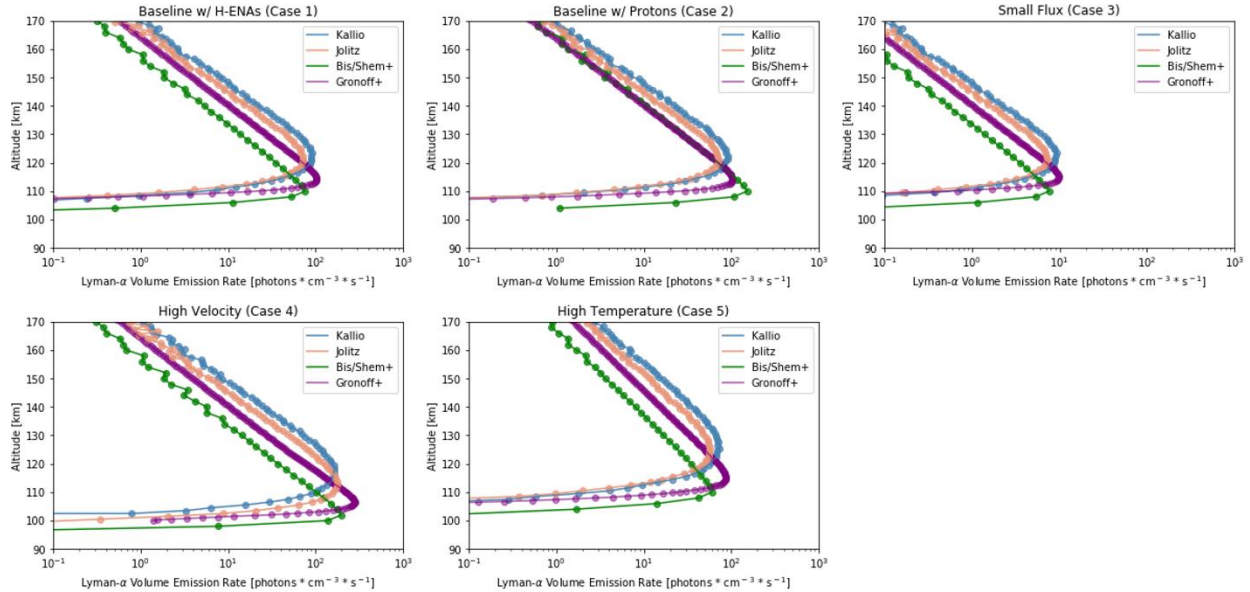
387 where z is altitude, n_{ref} is the number density at a reference altitude, z_{ref} is the chosen reference
 388 altitude (in this case, 120 km), and H is the CO₂ scale height. Here we assume $n_{\text{ref}} = 1 \times 10^{11} \text{ cm}^{-3}$
 389 at 120 km, and H is calculated for each temperature range using a value of $g = 3.46 \text{ m/s}^2$ (i.e., g
 390 at the reference altitude of 120 km). The calculated scale height values for the low and high
 391 temperature cases were 10.4 km and 13.1 km, respectively.

392

3.4. Results of Step 1-A

393 The results of the inter-model comparison in Figure 1 show many similarities between
 394 the different modeled proton aurora volume emission rates (VERs), with the results of the Jolitz
 395 and Kallio models exhibiting the most similarities. Interestingly, most models predict similar
 396 trends in the relative changes observed between each of the five representative cases. There is a
 397 large range in the proton aurora peak altitudes between the models, with the
 398 Bisikalo/Shematovich *et al.* model consistently predicting the lowest peak altitudes and the
 399 Gronoff *et al.* model predicting the second lowest. The peak altitudes in the Jolitz and Kallio
 400 models are consistent with each other in nearly every case, with the exception of the high
 401 velocity case (Case 4), where the Jolitz model predicts a slightly lower peak altitude than the

402 Kallio model. The Gronoff *et al.* model also consistently predicts the largest peak VERs in each
 403 case (with the exception of Case 2, where the Bisikalo/Shematovich *et al.* model predicts the
 404 largest peak VERs). Almost all of the models show no difference in the proton aurora profile
 405 (*i.e.*, VER or altitude) based on varying the type of incident particle at the top of the atmosphere
 406 (*i.e.*, H-ENA or proton; compare Case 1 and Case 2 profiles); the only exception being the
 407 Bisikalo/Shematovich *et al.* model, which predicts a slight increase in the VER of the proton
 408 aurora profile for protons rather than H-ENAs as the incident particle. The similarities between
 409 Cases 1 and 2 suggest that most models do not predict significant differences between a H-
 410 induced Ly- α emission and a proton-induced Ly- α emission in the proton aurora profile.



411

412 *Figure 1: Simulated Ly- α volume emission rates of proton aurora at different altitudes from each model in this study for the five*
 413 *representative input cases in the inter-model comparison step of the campaign (Step 1-A). The two input parameters that have the*
 414 *most significant effect on the results are the incident solar wind flux and velocity. See Table 1 for the input parameters used in*
 415 *each of the five representative cases.*

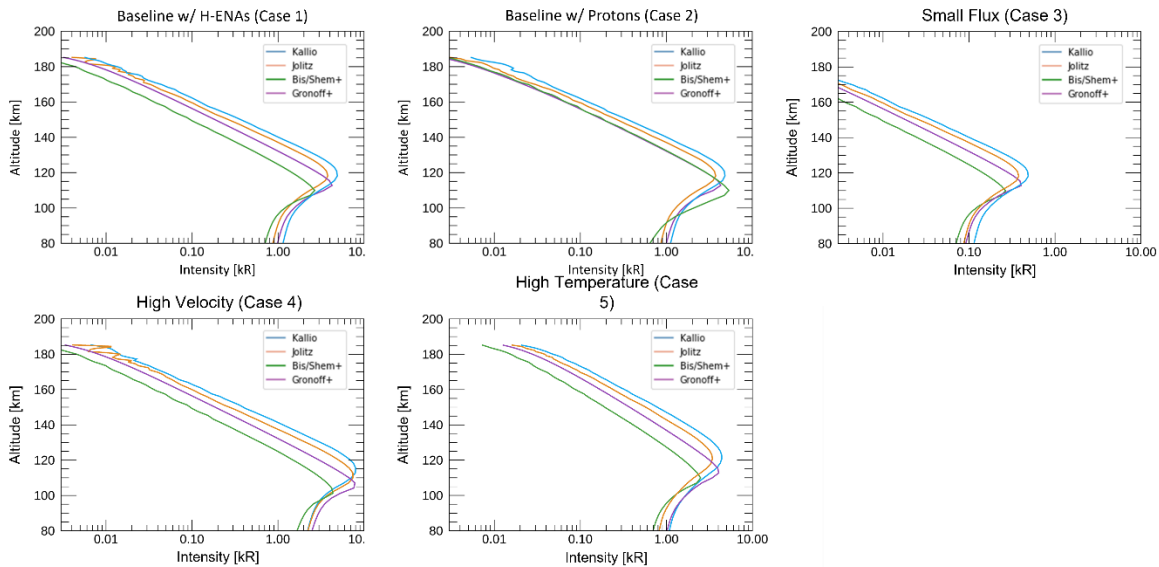
416 3.5. Results of Step 1-B

417 In Step 1-B we forward-model the results of Step 1-A into observation space (*e.g.*,
 418 perform a “line-of-sight” integration comparison). In this step we produce synthetic observations
 419 that would be made by MAVEN/IUVS given the computed volume emission rates. In so doing,
 420 the model results are converted from Ly- α volume emission rate (in units of photons/cm³s) to
 421 Ly- α intensity (in units of kilorayleighs, kR) using the previously described radiative transfer
 422 model. Using the same radiative transfer model to forward-model each simulation’s output in
 423 this step enables a more reliable cross-model comparison.

424 As shown in Figure 2, the results of Step 1-B further reveal similarities in the model
 425 intensities and peak altitudes for each of the five cases. We find consistently in each model that
 426 the two major variables that affect the proton aurora profile are the penetrating particle flux and
 427 the particle velocity. Decreasing the flux by an order of magnitude (Case 3) correspondingly
 428 decreases the Ly- α intensity by an order of magnitude. Similarly, doubling the particle velocity
 429 (Case 4) noticeably increases the peak intensity in each model and decreases the peak altitude by
 430 ~5-10 km. In the final representative input case of increasing the atmospheric temperature

431 (thereby changing the neutral atmospheric scale height) (Case 5), all of the models show a slight
 432 decrease in the Ly- α peak intensity and a change in the shape of the profile at higher altitudes
 433 (*i.e.*, the profile has a broader shape). Additionally, most of the models show an increase in the
 434 peak altitude by \sim 1-5 km in Case 5 (with the exception of the Bisikalo/Shematovich *et al.* model,
 435 which does not exhibit a change in the peak altitude due to the changing temperature/scale
 436 height). The differences in the profile observed in Case 5 are likely present because the volume
 437 emission rate, and therefore the unattenuated auroral brightness, scales inversely with the
 438 atmospheric scale height in order to conserve photon production in the atmosphere; this in turn
 439 causes the Ly- α brightness to appear more “spread out” across different altitudes in the proton
 440 aurora profile.

441 The consistency of these results between models confirms our understanding of the
 442 driving processes that have the most significant effect on the proton aurora profile. Particularly,
 443 we see in Cases 3 and 4 that the solar wind proton velocity and density (which also affect the
 444 particle energy and flux) are tremendously important in the formation of notable proton aurora
 445 events. Thus, we may extrapolate from the results that high velocity and/or density solar events
 446 (*e.g.*, coronal mass ejections and corotating interaction regions) will correspondingly create
 447 significantly enhanced proton aurora events. This finding is consistent with preliminary studies
 448 of proton aurora at Mars in which the observations were found to correspond with extreme solar
 449 activity events (*e.g.*, Ritter *et al.*, 2018).



450
 451 *Figure 2: Simulated Ly- α intensities from the inter-model comparison after running the results of Step 1-A through the radiative
 452 transfer (RT) model (Step 1-B), which forward-models the results into observation space (*e.g.*, performs a “line-of-sight”
 453 integration comparison). The model results more closely resemble each other after this step, but the dominant influencing factors
 454 identified in Step 1-A (Figure 1) are still present. See Table 1 for the input parameters used in each of the five representative
 455 cases.*

456 4. Inputs and Results for Data-Model comparison (Step 2)

457 4.1. Purpose and Description of Step 2

458 In the second step, we assess the robustness of each of the models based on their abilities
 459 to reproduce a typical proton aurora detection from the MAVEN/IUVS dataset. In undertaking

460 Step 2, different variables in the models were tuned to match proton aurora events in the
461 MAVEN/IUVS dataset. The models use relevant data inputs for a specific proton aurora event to
462 attempt to accurately reproduce the event. As in Step 1, the model results in Step 2-A are first
463 provided in their native formats, and subsequently forward-modeled into observation space in
464 Step 2-B using the radiative transfer model.

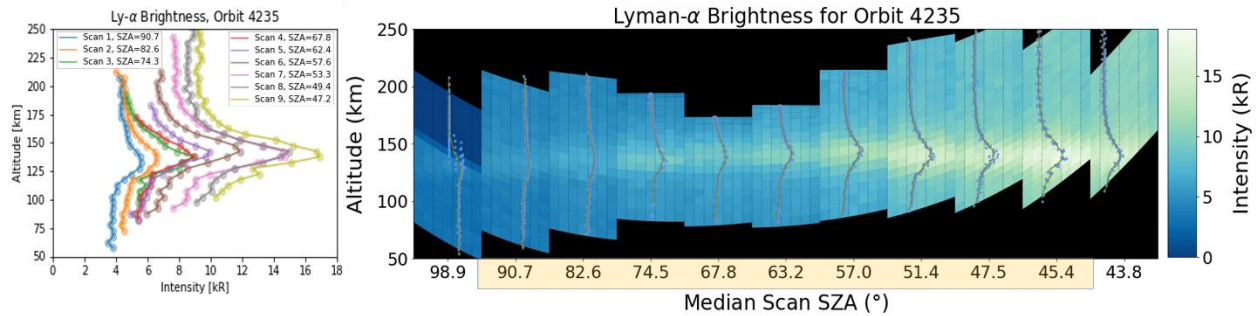
465 4.2. Description of Example Proton Aurora Event and MAVEN/IUVS Observations

466 For the data-model comparison stage of the campaign (Step 2), we selected an example
467 of a proton aurora event from the MAVEN/IUVS dataset that occurred during the periapsis
468 portion of MAVEN orbit #4235 (*i.e.*, December 3rd, 2016, starting at ~13:44 UTC). This
469 particular proton aurora event occurred at relatively low SZAs around southern summer solstice
470 ($L_s \sim 270^\circ$), a period of time exhibiting frequent proton aurora activity and increased dust activity
471 associated with the concurrent Martian dust storm season. Figure 3 shows the IUVS Ly- α
472 intensity data for this orbit. The left-hand plot of Figure 3 shows the Level 1C altitude-binned
473 Ly- α altitude-intensity profiles for each of the limb scans used in the study; and the right-hand
474 plot shows these profiles overlain on a synthetic image format of each of the IUVS limb scans
475 from this orbit (horizontal), showing the Ly- α intensity for each of the 21 IUVS mirror
476 integrations (vertical) and 7 spatial bins within each scan (*e.g.*, similar to Figure 2 in Deighan *et*
477 *al.*, 2018). Note that the scans are displayed as though they are contiguous even though
478 spacecraft and slit motions prevent full spatial coverage. There are eleven IUVS limb scans in
479 this orbit, but we use only the middle nine IUVS scans in this study (yellow highlighted scans in
480 Figure 3). In evaluating the robustness of each of the models in this step of the study, the model
481 results were compared with intensities and peak altitudes of the IUVS Ly- α profiles from these
482 nine scans.

483 There are minor peak altitude variations in IUVS Ly- α observations between scans
484 throughout this orbit. These minor altitude variations correspond with similar altitude variations
485 in the IUVS CO₂⁺ ultraviolet doublet emission (CO₂⁺ B 2 Σ \rightarrow X 2 Σ around 288 nm) (not
486 shown), suggesting the possible presence of waves and/or tides in the neutral atmosphere during
487 this orbit (*e.g.*, Lo *et al.*, 2015; England *et al.*, 2016). The likely presence of waves/tides in this
488 orbit is strengthened by similar observations in the MAVEN/NGIMS inbound CO₂ altitude-
489 density profile. We note, however, that altitude variations in the Ly- α and CO₂⁺ emissions are
490 less than 5 km, approaching the resolution limit of the observation; thus, the minor altitude
491 variations observed in the Ly- α peak intensity or CO₂ density during this orbit should not have
492 any significant influence on the modeled proton aurora profiles.

493 This particular proton aurora event exhibits an especially high orbit-mean Ly- α peak
494 intensity and emission enhancement (11.4 and 3.93 kR, respectively) as observed by IUVS. Also
495 notable during this orbit is a particularly high penetrating proton flux ($2.73 \times 10^6 \text{ cm}^{-2} \text{ s}^{-1}$)
496 observed by MAVEN's Solar Wind Ion Analyzer (SWIA) instrument (Halekas *et al.*, 2013).
497 SWIA observed a strong solar wind stream interaction during this orbit, resulting in this
498 especially high penetrating proton flux. The MAVEN periapsis during this orbit was in the
499 southern hemisphere on the dayside of the planet (with the exception of a few limb scan
500 observations near the terminator) (see Supplementary Figure S1 and Figure S2). Because the
501 spacecraft periapsis does not occur near any remanent crustal fields (Supplementary Figure S1),
502 we do not expect a significant influence (if any) from crustal fields during these observations.

503 The average upstream interplanetary magnetic field (IMF) magnitude and cone angle (*i.e.*, angle
504 off of the Mars-Sun line) during this orbit is ~ 10 nT and $\sim 45^\circ$, respectively.



505
506 *Figure 3: IUVS Ly- α intensity data of proton aurora observation used in the data-model portion of the campaign (Step 2). Left:*
507 *IUVS Level 1C altitude-intensity profiles for limb scans used in the study (MAVEN orbit #4235); SZA at the profile peak for each*
508 *limb scan is shown in the legend. Right: Altitude-intensity profiles overlain on top of a synthetic image format of Ly- α intensities*
509 *for each IUVS limb scan/mirror angle in this orbit (e.g., similar to Figure 2 from Deighan et al. 2018; see text for more details).*
510 *Note that the scans are displayed as though they are contiguous but spacecraft and slit motions prevent full coverage. Only the*
511 *central nine scans are used in this study (scans that are highlighted yellow at the bottom), and the SZA values shown at the*
512 *bottom correspond with the median SZA for each limb scan in the orbit.*

513 4.3. Background Subtraction of Coronal H Contribution from IUVS Ly- α Brightness

514 The Ly- α brightness observed in the IUVS data is created by contributions from not only
515 the non-thermal solar wind-derived H that produces proton aurora, but also from the thermalized
516 background coronal H. Thus, by subtracting out the background coronal H from the IUVS proton
517 aurora profiles, we are able to accurately compare the data with the model results. We perform
518 this coronal H background subtraction by first estimating the background coronal H brightness
519 during this time using IUVS limb scan profiles from a nearby orbit that exhibits little/less
520 evidence of enhancement due to proton aurora activity at a similar SZA (in this case we use orbit
521 #4229, as it exhibits the least contribution from proton aurora than any surrounding orbits).
522 These heuristic coronal Ly- α profiles are created by fitting an arcsine function to the upper- and
523 lower-most altitudes of the Ly- α profiles from the nearby orbit with little/less proton aurora
524 activity. Each heuristic profile of the estimated background Ly- α brightness due to the coronal H
525 in a given orbit is then subtracted out from each corresponding IUVS limb scan at a similar SZA
526 from the orbit of interest containing strong evidence of proton aurora (see Supplementary Figure
527 S3 for Ly- α profiles before and after background subtraction and heuristic coronal background
528 profiles used). This method is similar to the background subtraction methodology used by
529 Deighan *et al.* (2018) but differs in the determination of the background coronal H profile due
530 the absence of nearby orbits that completely lack proton aurora (*i.e.*, because of the before
531 mentioned near continuous proton aurora activity during the southern summer season). The
532 corrected intensities should then more closely reflect the H Ly- α contribution only from proton
533 aurora. In order to determine its effectiveness, this background coronal H subtraction technique
534 was tested on numerous other IUVS proton aurora detections and found to be a highly effective
535 empirical method for isolating the proton aurora contribution to the IUVS Ly- α observations.
536 However, as this methodology estimates a heuristic background coronal H by assuming
537 minimal/no changes in the neutral atmosphere between multiple orbits, there will be inaccuracies
538 in the corrected proton aurora profiles; we estimate these inaccuracies to be only a fraction of a
539 kR at most.

540 As shown in Supplementary Figure S3, the IUVS Ly- α intensities are reduced
 541 significantly due to this background-subtraction routine (by nearly 10 kR at low SZAs), but the
 542 shape of the profiles around the proton aurora profile peak (*i.e.*, between ~110-150 km) does not
 543 change. The profile peak altitudes typically also do not change as a result of this background
 544 subtraction methodology, provided that the peak altitudes of the proton aurora orbit profiles are
 545 not significantly different from those of the background subtraction orbit profiles (*i.e.*, the nearby
 546 orbit with little/less enhancement due to proton aurora). However, because of a slight difference
 547 in peak altitudes between the orbit considered in this study and the orbit used for the background
 548 subtraction routine (*i.e.*, orbits 4235 and 4229, respectively) at the lowest SZA profile, the peak
 549 altitude of the SZA ~45° background subtracted profile has been (artificially) slightly shifted
 550 down by ~5 km.

551 4.4. Assumptions/Constraints for Step 2

552 In Step 2, the models used inputs drawn from observations made by MAVEN (discussed
 553 more below). We apply many of the same constraints and assumptions as those applied in Step 1
 554 (*i.e.*, assuming a monoenergetic incident particle beam and monodirectional incident particle
 555 movement, and constraining the cross section processes used). One notable difference in Step 2
 556 is that the models produced outputs at a range of solar zenith angles (*i.e.*, not just at the subsolar
 557 point) in order to simulate the different SZAs of each of the IUVS limb scans in this orbit. As in
 558 Step 1, we exclude any effects due to electric or magnetic fields.

559 In order to additionally simplify the inputs for this step, all models assume that the
 560 incident particle population is composed entirely of H-ENAs at the top of the atmosphere (*i.e.*,
 561 assuming an initial penetrating proton component equal to zero). Based on our findings in Step 1,
 562 the proton aurora profile does not significantly change in most models when assuming 100%
 563 protons or 100% H-ENAs. Thus, this assumption of particle composition should not significantly
 564 affect the final results. The initial H-ENA flux ($F_{\text{H-ENA}}$) is approximated using the equation:

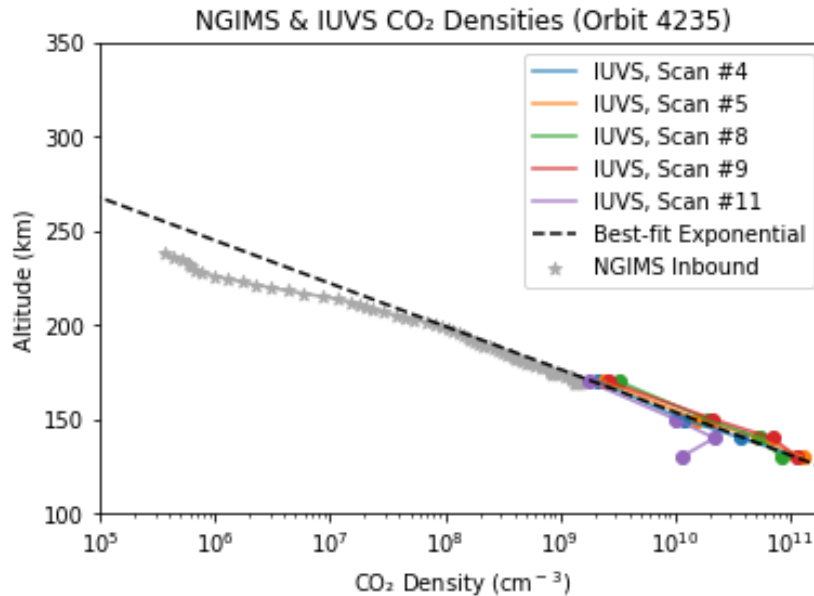
$$565 F_{\text{H-ENA}} = F_{\text{pp}} \times 13.5, \quad (2)$$

566 where F_{pp} (the orbit mean penetrating proton flux derived from SWIA) equals $2.73 \times 10^6 \text{ cm}^{-2} \text{ s}^{-1}$
 567 in this orbit, and 1/13.5 is the approximate fraction of the incoming beam of H-ENAs that is
 568 converted to protons. This conversion value was determined based on previous SWIA
 569 observations and the relevant energy-dependent electron stripping and charge exchange cross
 570 sections (*e.g.*, Halekas *et al.*, 2015; Halekas, 2017), assuming that at the point when H-H⁺
 571 equilibrium is reached in the collisional atmosphere (*i.e.*, the location of the SWIA measurement)
 572 the mix is ~92.5% ENAs and ~7.5% protons (*i.e.*, the equilibrium fractionation for the relevant
 573 cross sections at 1 keV).

574 Another constraint carried over from Step 1 is that all models used the same
 575 representative CO₂ density (*i.e.*, a 1 km altitude-binned CO₂ number density profile). However,
 576 in Step 2, the theoretical CO₂ density line profile is created based on neutral densities from two
 577 MAVEN instruments observing at different altitude ranges during this orbit: IUVS and the
 578 Neutral Gas and Ion Mass Spectrometer (NGIMS) (Mahaffy *et al.*, 2015). We note that although
 579 NGIMS data are acquired during both the inbound and outbound portions of the orbit, we restrict
 580 this study to include only inbound data, due to instrument artifacts which have been found to
 581 artificially increase CO₂ densities in NGIMS outbound data (*e.g.*, Stone *et al.*, 2018). The IUVS
 582 and NGIMS neutral densities are consistent with each other within the limited overlapping
 583 altitude range of the two instruments (*i.e.*, at a reference altitude of 170 km, the NGIMS CO₂

584 density is $\sim 1.48 \times 10^9 \text{ cm}^{-3}$, and the smallest derived CO_2 density from different IUVS limb
 585 scans is $\sim 1.74 \times 10^9 \text{ cm}^{-3}$).

586 Figure 4 shows the theoretical CO_2 profile for Step 2, which is created by fitting an
 587 exponential to the IUVS and inbound NGIMS data using equation (1). In this case, $n_{\text{ref}} =$
 588 $1.1 \times 10^{11} \text{ cm}^{-3}$ (the average IUVS density at reference altitude z_{ref}), $z_{\text{ref}} = 130 \text{ km}$ (the minimum
 589 altitude observed by IUVS during this orbit). The CO_2 scale height was estimated by varying the
 590 temperature value until an appropriate fit was achieved (using a value of $g = 3.41 \text{ m/s}^2$ at 130
 591 km); a temperature of 180 K was found for the best-fit line.



592
 593 Figure 4: Empirically-derived theoretical CO_2 profile used by models for the data-model comparison (Step 2). This profile was
 594 created by fitting a best-fit exponential to the derived IUVS and measured NGIMS inbound data from this MAVEN orbit.

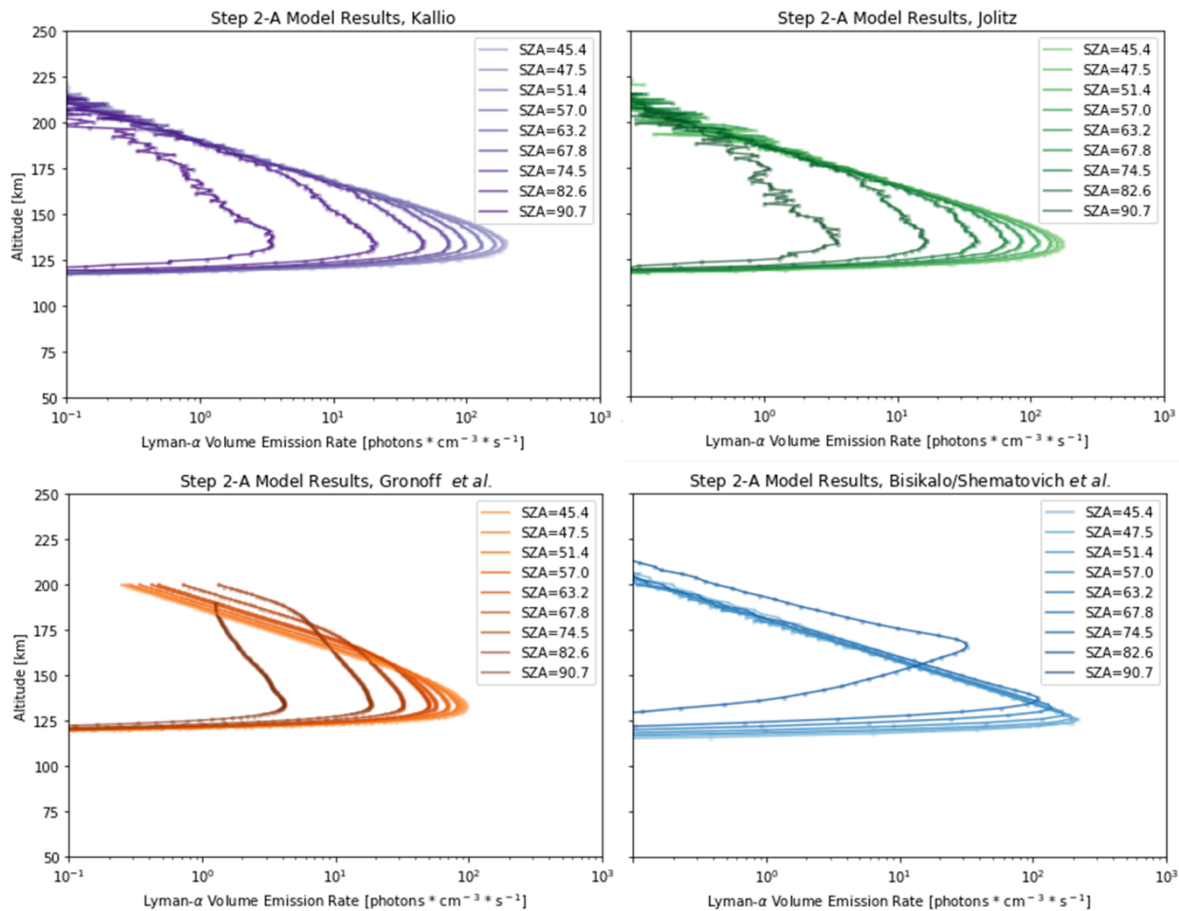
595 4.5. Results of Step 2-A

596 The results of Step 2-A show that all models simulate the input data to within less than an
 597 order of magnitude of the same volume emission rates (VERs) (Figure 5). As in Step 1, the
 598 results of Step 2-A also show that the Jolitz and Kallio simulations exhibit the most similarities
 599 to each other in terms of VERs and peak altitudes. The Gronoff *et al.* model results exhibit
 600 relatively low VERs compared with other models.

601 In Step 1, we used the models to simulate a proton aurora profile at a single SZA (*i.e.*, the
 602 subsolar point). However, in Step 2, each model simulated proton aurora profiles at numerous
 603 SZAs between $\sim 45^\circ$ - 90° . Thus, in Step 2 we are able to observe the decrease in Ly- α proton
 604 aurora brightness associated with increasing SZA. The proton aurora brightness appears to
 605 monotonically decrease in the Kallio, Jolitz, and Gronoff *et al.* simulations (particularly at low
 606 SZAs), but in the Bisikalo/Shematovich *et al.* simulation results the decrease is more gradual at
 607 lower SZAs (and pronounced at higher SZAs).

608 We note that the Bisikalo/Shematovich *et al.* Monte Carlo calculations for the two
 609 highest SZA profiles (*i.e.*, SZA= 82.6° and 90.7°) resulted in practically no Ly- α excitations
 610 (hence their absence on the plots in Figure 5 and Figure 6). The Bisikalo/Shematovich *et al.*

611 model results also exhibit relatively low peak altitudes at lower SZAs in comparison with other
 612 models; however, this model is the only one showing variability in the peak altitudes between
 613 SZA profiles. In this 1-D kinetic model, Ly- α photons are excited in local collisions of H-ENAs
 614 with the ambient atmospheric gas and the VERs are accumulated for the projection velocities of
 615 H-ENAs into the given SZA direction. In the case of high SZAs, the Ly- α excitations are caused
 616 mainly by the H-ENAs moving in the tangential trajectories relative to the upper atmosphere
 617 (*i.e.*, by H-ENAs which do not penetrate deep into the atmosphere). This results in: a) very low
 618 values of Ly- α VERs for high SZAs (especially for runs with SZA=82.6° and 90.7°); and b) an
 619 increase of the peak height of the profiles with SZA (*i.e.*, because the kinetic energy of collisions
 620 becomes lower for the excitation collisions along the tangential trajectories of the H-ENAs).



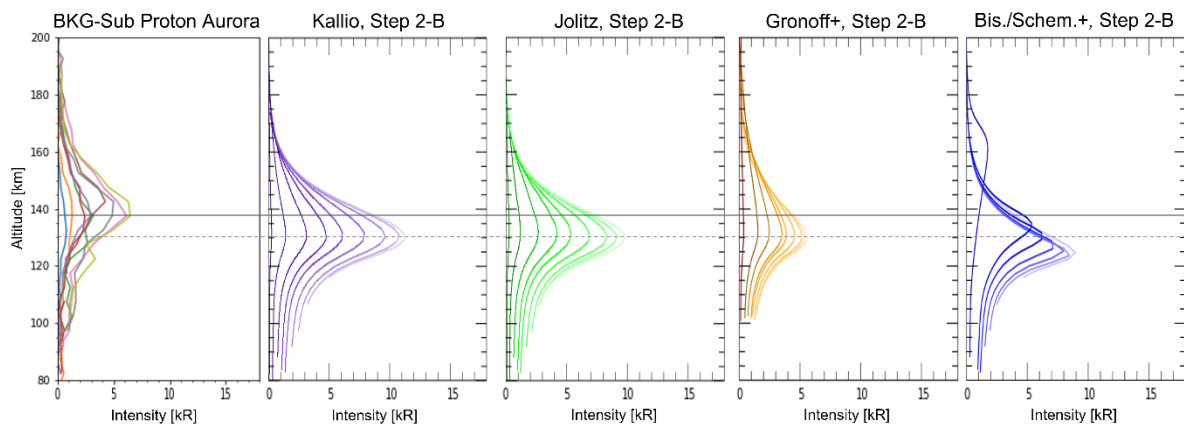
621
 622 *Figure 5: Simulation results from the data-model comparison step of the campaign (Step 2-A), showing proton aurora altitude-*
 623 *volume emission rate (VER) profiles from each model for the specified input parameters and SZAs. Most model results display*
 624 *similar peak altitudes and VERs agree with each other to within less than an order of magnitude. Note that SZA is decreasing*
 625 *from left-to-right between profiles in each panel.*

626 4.6. Results of Step 2-B

627 Forward-modeling the simulation results using the radiative transfer model in Step 2-B allows a
 628 more direct comparison between the model results and the IUVS data. In so doing, we find
 629 through Step 2-B that the models effectively reproduce the general shape of the data, with some
 630 models overestimating and some underestimating the proton aurora brightness (Figure 6). All of
 631 the peak altitudes from the model results are ~5-15 km lower than the observed peak altitudes.
 632 The simulated intensities of the Gronoff *et al.* and Bisikalo/Shematovich *et al.* model results for

633 the low SZA profiles (*i.e.*, profiles on the right-most side of each plot) are ~ 1 - 1.5 kR higher and
 634 lower (respectively) than the proton aurora intensities observed in the data for similar SZA
 635 profiles. However, at high SZAs, all three models for which profiles exist appear to simulate the
 636 data intensities effectively. The Kallio and Jolitz model intensities overestimate the data by a few
 637 kR at low SZAs, while the Gronoff *et al.* model intensities underestimate by a few kR. At low
 638 SZAs, the Bisikalo/Shematovich *et al.* model intensities closely correlate with the data
 639 intensities, but still slightly overestimate the data; however, the Bisikalo/Shematovich *et al.*
 640 intensities underestimate the data at high SZAs. While all models effectively simulate the shape
 641 and SZA variability of the data profiles, none of the model intensities match the data exactly
 642 (possible reasons for this discrepancy are discussed in the following section).

643 Significant peak altitude discrepancies between the models and the data are present in
 644 every model. This altitude discrepancy suggests that other processes/assumptions are not fully
 645 accounted for or understood in our evaluation of the results. In the following section, we
 646 examine numerous possible parameters that may contribute to the observed discrepancies
 647 between the data and the models.



648

649 *Figure 6: Simulation results for the data-model comparison after running the results through the radiative transfer model (Step*
 650 *2-B). The background-subtracted (*i.e.*, after subtracting out the theoretical “background” coronal H contribution) altitude-*
 651 *intensity profiles for this orbit are shown on the far left plot for comparison. The simulated proton aurora Ly- α intensities from*
 652 *each of the model results closely correlate with the data. However, note that there is still a discrepancy between the average peak*
 653 *altitude of the data profiles (solid grey horizontal line) and the average peak altitude of the model profiles (dashed grey*
 654 *horizontal line). Note also that the SZA of the observations is decreasing from left to right in all plots from SZA $\sim 90^\circ$ to SZA $\sim 45^\circ$*
 655 *(*i.e.*, moving toward the subsolar point), as shown in Figure 3 and Figure 5 legend.*

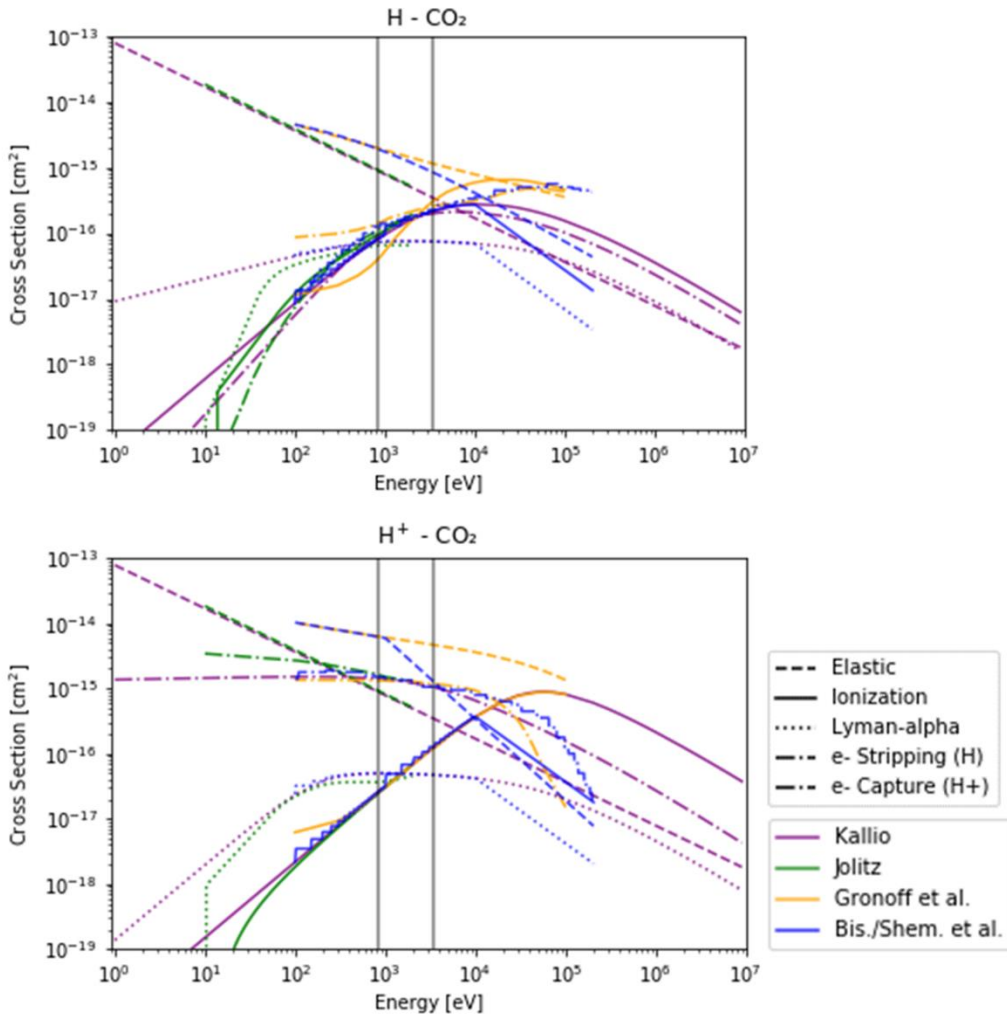
656 5. Discussion of parameters affecting model differences and data-model discrepancies

657 5.1. Cross Section Processes and Scattering Angle Distributions

658 Differences in cross section and DSCS values are a probable partial contributor to the
 659 differences in the results simulated by each model. While the models in this study utilize the
 660 same five processes, most models do not use the same cross sections (see Figure 7 and
 661 Supplementary Table S1 for details). As shown in Figure 7, these values can change significantly
 662 with varying energy ranges. The cross section values used in each model agree to within less
 663 than an order of magnitude of each other for the relevant energy range in this study (*i.e.*, 100 eV
 664 – 2 keV). The most variable cross section across the models were those used for elastic
 665 collisions, with elastic cross sections used by the Bisikalo/Shematovich *et al.* and Gronoff *et al.*
 666 models exceeding those used by the Kallio and Jolitz models by a factor of ~ 5 - 8 . These

667 differences can cause notable inter-model variability. Since many processes have not been
668 measured in a laboratory for proton/H collisions with CO₂, an interpolated or substitute value is
669 used for protons/H with O₂ or N₂. Particularly few measurements of protons with CO₂ are
670 available for Ly- α . Comparable cross section values are a likely cause for the similarities
671 observed between the Jolitz and Kallio results, and also a likely cause for the minor variability
672 between these two models in the data-model comparison (*i.e.*, the Jolitz model uses smaller Ly- α
673 cross sections at low energies and exhibits intensities that are 1-2 kR smaller than those of the
674 Kallio model at low SZAs).

675 Different implementations of scattering can also cause inter-model variations. A model
676 that assumes that a particle travels in the same direction before and after a collision (“forward
677 scattering”) will predict deeper particle penetration than a model that predicts variability in
678 scattering angle. Introducing even a small probability of non-forward scattering reduces the
679 precipitating flux and resulting emission rate. This is done by converting measured DSCS into a
680 phase function evaluated during a model run. In this study, each model uses different ways to
681 predict scattering (see supplementary material Text S1-S4 for detailed model descriptions).
682 Kallio and Jolitz use the same phase function to predict non-zero scattering angles after elastic
683 collisions, while all other collisions are assumed to be forward scattering. This, in tandem with
684 the same model approach (3-D Monte Carlo) likely contributes to their similar model
685 predictions. In contrast, the two 1-D kinetic Boltzmann solver models have slightly different
686 scattering models. Gronoff *et al.* uses a screened Rutherford phase function with a fixed
687 screening parameter in charge transfer and elastic collisions and assumes forward scattering in
688 ionization collisions. Bisikalo/Shematovich *et al.* uses the same assumptions for all collisions
689 except charge transfer, for which the model uses energy-dependent DSCS. The inclusion of non-
690 forward scattering in these 1-D models could be responsible for the lower intensities predicted by
691 these models compared to those predicted by the 3-D Monte Carlo models.



692
693
694
695
696

Figure 7: Available cross section values used by each modeling team (denoted by color) for the five different overlapping cross section processes considered in this study (denoted by line style). The solid vertical lines (grey) indicate the energy ranges evaluated in the representative cases in Step 1 assuming average (400 km/s) and high (800 km/s) solar wind velocities. See Supplementary Table S1 for more information regarding the cross section processes and relevant references in each model.

697 5.2. Data Quality and Caveats

698 In addition to the possible sources of discrepancy in the model assumptions, we must also
699 consider possible caveats associated with the datasets. Because IUVS is a remote sensing
700 instrument, its limb scan observations are created by integrating along the line of sight of the
701 instrument. However, the SWIA penetrating proton fluxes are measured *in situ* during periapsis,
702 and the orbit averaged value is used in this study. Because of the uniform nature of the processes
703 creating proton aurora across the dayside of the planet it is appropriate to combine these datasets;
704 nevertheless, there may be spatial and/or temporal discrepancies between these observations,
705 even though the data were acquired during the same MAVEN orbit.

706 Secondly, because IUVS Level 1C (L1C) data are processed and altitude-binned, we note
707 that minor discrepancies may be introduced in the Ly- α intensities during the data reduction
708 process. Calibrated IUVS L1C data are reported with a systematic uncertainty between ~ 10 -20%.
709 As the results of this study are sensitive to the absolute calibration of the instrument, we must

710 also consider any possible uncertainties in the IUVS reported intensities as a potential source of
711 discrepancy in the model-data comparison.

712 5.3. Other Assumptions

713 There are a number of additional assumptions in this study that may have led to
714 discrepancies between the models and the data. First, numerous data-driven assumptions are
715 made in creating the theoretical CO₂ density profile for Step 2. Any of three variables could be
716 altered that could in turn significantly affect the proton aurora profile: the energy of the incident
717 particles, the density of the atmosphere at the reference altitude, or the neutral atmospheric scale
718 height. All of these variables affect the peak altitude of the proton aurora profile, while changing
719 the scale height and energy also affects the profile peak intensity (more specifically, changing
720 the scale height can also affect how broad/narrow the profile shape becomes). Observations
721 made by MAVEN/SWIA during this orbit provide confidence that the calculation of particle
722 energy (based on average penetrating proton velocity) and the assumption of monoenergetic
723 particle behavior are appropriate/accurate, and therefore do not significantly affect the results.
724 However, in this study we determine the atmospheric density at the reference altitude (130 km)
725 by extrapolating from the average derived IUVS Level 2 CO₂ density at 130 km. Because the
726 spherically symmetric CO₂ density profile used by modelers in this study is theoretically derived,
727 inaccuracies in the assumed quantities for reference density or scale height would lead to an
728 inaccurate representation of the atmospheric density profile during this time. Thus, it is possible
729 that the CO₂ density profile is not entirely accurate in representing the atmosphere at this time,
730 possibly contributing to some of the discrepancies observed in the data-model comparison.
731 Moreover, only one neutral species (CO₂) is considered in our models, whereas other minor
732 species (*e.g.*, CO, O₂ and O) should also contribute to some extent to the observed profiles (in a
733 potentially important way, depending on altitude and latitude/longitude). Since H⁺/H cross
734 sections can vary significantly depending on the target neutral species (both in peak energy and
735 intensity), the modeling results presented may be modified further if these species are included.
736 We note, however, that because CO₂ is the overwhelmingly dominant species in the Martian
737 atmosphere, the inclusion of minor species should not alter any of the primary findings presented
738 in this study (but may decrease the observed discrepancies between the data and models). Such
739 an added complexity is outside the scope of the present study and a more in-depth investigation
740 of the inter-model's sensitivity to the neutral atmosphere composition is left for the future.

741 For simplicity in Step 2 we assume that the precipitating particle population at the top of
742 each model atmosphere is entirely composed of H-ENAs. Although the incident particle
743 population is indeed comprised of a fractionated portion of both ENAs and protons, this
744 simplified assumption is preferred over a non-empirical assumption of an estimated fractionation
745 ratio. Moreover, as the results in Step 1 do not significantly change in most models based on the
746 assumption of an entirely H-ENA- or proton-rich population, we would not expect the effects of
747 this assumption on its own to have a significant impact on the final results. One potential
748 exception may be for the Bisikalo/Shematovich *et al.* results in which the peak intensity
749 somewhat increases if a particle population of entirely protons is assumed (as seen in Step 1-A
750 and 1-B). Because the Bisikalo/Shematovich *et al.* results showed slight variability based on the
751 assumed incident particle population, it is possible that the intensities in their model results
752 might be larger if this assumption is changed (which may cause their simulated intensities to
753 more closely resemble those of the Kallio and Jolitz models, but to further overestimate the data
754 intensities in Step 2).

755 The chosen method for calculating the ENA flux may be a contributor to the observed
756 discrepancies between the data and model intensities. The H-ENA flux used in Step 2 is
757 calculated as an empirically derived multiple of the orbit-averaged SWIA penetrating proton
758 flux. While this ratio is supported by previous SWIA observations (*e.g.*, Halekas *et al.*, 2015;
759 Halekas, 2017), the value can vary based on seasonal or other changes (*e.g.*, the solar wind
760 proton flux, the neutral atmospheric scale height, or the location of the bow shock). As
761 determined in Step 1, decreasing the flux by an order of magnitude (which is the typical
762 variability observed throughout a Martian year, *e.g.*, Halekas, 2017) will correspondingly
763 decrease the proton aurora peak intensity by an order of magnitude. Thus, although the method
764 used to calculate the ENA flux is believed to be an accurate and statistically robust
765 approximation, any major deviation from the statistical norm of local conditions during this orbit
766 would cause discrepancies in accurately calculating the H-ENA flux.

767 Another possible contributor to the data-model discrepancies is the assumption of the
768 monodirectional movement of the incident particles in the atmosphere. We include a terminology
769 note here that in specifying “monodirectional” particle movement, we refer to the bulk velocity
770 (*i.e.*, average speed and direction) of the precipitating particles. All modeling teams represented
771 the incident precipitating particles as having a velocity fixed in magnitude (*e.g.*, 400 km/s and
772 800 km/s) and direction (anti-sunward). However, in reality the incident solar wind has nonzero
773 temperature, and has a broader variability than modeled. While some model teams investigated
774 the potential effects of this variability on the proton aurora profile (*e.g.*, Supplementary Figure
775 S4), the results are preliminary and will be reviewed in further detail in a future study.

776 In this study we do not consider the effects of electric or magnetic fields (*i.e.*, IMF,
777 induced, and/or crustal magnetic fields) on proton aurora. While most of the models do not
778 predict any likely significant change on the proton aurora profile caused by magnetic fields, a
779 previous modeling study by Gérard *et al.* (2019) (which utilized the Bisikalo/Shematovich *et al.*
780 proton/hydrogen precipitation model) predicted a decrease in the peak brightness of the proton
781 aurora profile in the presence of an induced magnetic field (*e.g.*, tens of nT). Comparatively, a
782 recent study by Henderson *et al.* (2022) that evaluated the effects of magnetic fields on
783 MAVEN/SWIA observations of penetrating protons suggests that only the very strongest
784 magnetic fields (*e.g.*, strengths greater than 200 nT) are expected to have a notable influence on
785 penetrating proton fluxes (*i.e.*, they did not find a significant influence for magnetic field
786 strengths on the order of 10 nT). Since the IMF magnitude during the MAVEN orbit included in
787 this study is non-negligible (*i.e.*, ~10 nT), it is possible that excluding magnetic/electric fields
788 from our study may contribute to some of the observed model-data discrepancies. However,
789 further analysis is required in order to understand the effects of magnetic fields (and variability
790 in field strengths) on the proton aurora profile.

791 Lastly, we also do not consider the effects of particle backscattering on the results of this
792 study. Because recent SWIA studies have shown that a significant portion of the incident particle
793 population can be backscattered (Girazian and Halekas, 2021), this factor could thereby
794 contribute to the data-model discrepancies (*e.g.*, potentially causing a lower observed proton
795 aurora brightness in the data than what is predicted by models). However, determining the
796 relative abundances of the forward- and back-scattered particle populations is outside the
797 purview of this study and thus the potential impacts on model results are not quantified herein.

798 5.4. Unique model Capabilities and Insights

799 As previously stated, the purpose of this campaign is not to identify the best or most
800 accurate model in the study, but rather, to characterize the ways in which each of the models
801 uniquely excel. In this section we identify aspects of each model that make them distinctively
802 capable in simulating proton aurora observations, as well as reasons for strong
803 agreement/disagreement between the models.

804 A few important aspects to consider are the cross sections used in each model, the
805 differences in the way the 3-D and 1-D solvers work, and how the relevant physics is treated.
806 The Monte Carlo solving techniques (*e.g.*, collision by collision determinators) and cross
807 sections used in the Kallio and Jolitz models are very similar (*e.g.*, Figure 7 and Supplementary
808 Table S1), leading to the observed similarities in their model results. In contrast to these two
809 models, the Bisikalo/Shematovich *et al.* and Gronoff *et al.* models generate outputs by solving
810 coupled proton-hydrogen kinetic Boltzmann transport equations. The Bisikalo/Shematovich *et al.*
811 model, which also uses Monte Carlo solving techniques, likely exhibits different results than
812 the former two models because of the use of different cross sections and 1-D model
813 dimensionality. The Gronoff *et al.* kinetic transport model uses cross section values different
814 than those of other models and a unique 1-D multistream kinetic transport solver. Nevertheless,
815 considering the variety of assumptions and technical implementations included in each model, it
816 is striking how well all of the models agree with each other as well as with the data.

817 The Bisikalo/Shematovich *et al.* model is the only one to simulate results that display
818 variability with SZA in the profile peak altitude: at low SZAs their simulated peak altitudes are
819 the furthest from the data peak altitudes, but at some higher SZAs their simulated peak altitudes
820 are closest to those of the data out of all models. Their model is unique in its incorporation of the
821 physics associated with this variability. However, we note that the peak altitudes simulated by
822 their model at very high SZAs are considerably higher than those typically observed for proton
823 aurora (*e.g.*, Hughes *et al.*, 2019).

824 The differences between the model results in the data-model comparison step
825 demonstrate the capabilities, assumptions, and methodologies of each of the models. The
826 Gronoff *et al.* and Bisikalo/Shematovich *et al.* models seem to be especially apt at approximating
827 the data intensities at lower SZAs (although the Bisikalo/Shematovich *et al.* simulated intensities
828 diverge the most at high SZAs). All models predict results which appropriately represent the
829 decrease in Ly- α brightness with increasing SZA: the Kallio, Jolitz, and Gronoff *et al.* models
830 appear to most accurately simulate this intensity falloff. The Bisikalo/Shematovich *et al.* model
831 appears to be particularly efficient at simulating the relative intensity differences between
832 profiles at lower SZAs, but the Jolitz model appears to be most consistently efficient across all
833 SZAs. While all models are effective at simulating the data, none of the four particle
834 precipitation models - which results are then run through the radiative transport model - can
835 exactly reproduce the analyzed Ly- α peak intensities and altitudes measured by the IUVS
836 instrument during MAVEN orbit 4235. This may indicate that the input parameters may not
837 accurately represent the situation in the presented case, that the cross sections used may contain
838 noticeable inaccuracies, and/or that some physical processes which are not included into the
839 models play an important role in proton aurora formation.

840 6. Conclusions and Future Work

841 The results of this modeling campaign provide a new understanding of the primary
842 factors influencing variability in Martian proton aurora. We identify the relative importance of

843 different input parameters on the proton aurora profile, finding the solar wind particle flux and
844 velocity to be the most influential parameters affecting the profile shape, brightness, and peak
845 altitude. Through undertaking this comparative study, we better constrain the driving processes
846 of proton aurora as characterized by each contributing model; additionally, we determine the
847 influence of model capabilities, solving techniques, and input assumptions on effectively
848 reproducing proton aurora observations, and the dominant physics that needs to be incorporated
849 in future modeling studies in order to accurately represent these events. Moreover, the results of
850 this study are applicable more broadly than proton aurora at Mars, as similar auroral processes
851 could occur on any planetary body that exhibits an extensive neutral H corona. Modeling studies
852 such as this one are particularly important in efforts to study planetary bodies with minimal
853 observations or where data are not available, both within our solar system and beyond (*e.g.*,
854 Venus, comets, and exoplanets).

855 In a future study, we aim to address the effects of magnetic and electric fields on proton
856 aurora. It will also be important to quantify the effect of the backscattered penetrating particle
857 population on the proton aurora profile; since the models in this study can readily take into
858 account collisional angular redistributions, incorporating these effects into the models would be
859 feasible and relevant. Evaluating the effects of the monodirectional particle movement
860 assumption (*e.g.*, by varying the incident particle bulk velocity/temperature) should also be
861 considered in a future study. We note that this study depends strongly on consideration of the
862 efficiency of charge exchange between protons in the undisturbed solar wind and H in the
863 extended corona (as this is an upper boundary for calculations due to the precipitation of H-
864 ENAs). Therefore, another possible next step for this campaign could be to consider the
865 variations present in an energy spectrum of incident H atoms and protons (*i.e.*, an energy
866 spectrum that is not monoenergetic). Additionally, major changes in the neutral atmospheric
867 scale height (*e.g.*, local or global dust storms) can affect absorption by CO₂ on the bottom side of
868 the proton aurora profile. Because absorption of Ly- α by CO₂ becomes significant below the
869 peak of the proton aurora Ly- α emitting layer, it can have a non-trivial effect on proton aurora
870 modeling efforts, potentially causing apparently lower peak intensities and higher peak altitudes
871 in proton aurora profiles. We plan to address these effects of CO₂ absorption on the proton
872 aurora profile in more detail. A future study could also potentially include creating a more
873 detailed neutral model atmosphere to use in the models (*e.g.*, including SZA variability), or
874 perhaps looking at nadir observations of proton aurora, which may help to bridge the gap
875 between *in-situ* and remote sensing observations. Finally, it would be interesting to expand our
876 analysis to include an “atypical” example of a proton aurora event in the data-modeling portion
877 of the campaign (*e.g.*, spatially and/or temporally varying, nightside detections, etc.).

878 The MAVEN mission continues to make new and exciting observations of Martian
879 proton aurora, and new Mars missions with UV instrument capabilities are also beginning to
880 make contemporaneous observations of these events. As the current solar cycle increases toward
881 solar maximum (a period corresponding with larger and more frequent solar activity), we
882 anticipate that the intensity and frequency of proton aurora events at Mars will also increase
883 correspondingly (*e.g.*, Hughes *et al.*, 2019). Thus, it is imperative in our efforts to study proton
884 aurora that we first develop a firm knowledge of the physics and driving processes through
885 modeling these events; this understanding will provide important context for future efforts to
886 effectively model new and unique auroral observations at Mars.

887

888 **Acknowledgments and Data Availability**

889 The MAVEN mission is supported by NASA through the Mars Exploration Program in
 890 association with the University of Colorado and NASA's Goddard Space Flight Center. The
 891 work of GG and BH was supported by the NASA grant 80NSSC20K1348. CSW is funded by
 892 Austrian Science Fund (FWF) project P35954-N. EK acknowledges support from the Academy
 893 of Finland (Decisions No. 348784 and No. 310444). VS and DB acknowledge the financial
 894 support of the Russian Science Foundation, grant # 22-12-00364. JCG acknowledges support
 895 from the PRODEX program of ESA managed with the help of the Belgian Federal Scientific
 896 Policy Office (BELSPO).

897 In this study we use MAVEN/IUVS Level 1C version 13 altitude-binned periapsis data.
 898 This work utilized the RMACC Summit supercomputer, which is supported by the National
 899 Science Foundation (awards ACI-1532235 and ACI-1532236), the University of Colorado
 900 Boulder, and Colorado State University. The Summit supercomputer is a joint effort of the
 901 University of Colorado Boulder and Colorado State University.

902 All daytime Level 1C IUVS data products are publicly available from the Planetary
 903 Atmospheres node of the Planetary Data System (PDS) ([https://pds-
 904 atmospheres.nmsu.edu/data_and_services/atmospheres_data/MAVEN/maven_iuvs.html](https://pds-atmospheres.nmsu.edu/data_and_services/atmospheres_data/MAVEN/maven_iuvs.html)).
 905 Similarly, MAVEN/SWIA ([https://pds-
 906 atmospheres.nmsu.edu/data_and_services/atmospheres_data/MAVEN/swia.html](https://pds-atmospheres.nmsu.edu/data_and_services/atmospheres_data/MAVEN/swia.html)) and
 907 MAVEN/NGIMS ([https://pds-
 908 atmospheres.nmsu.edu/data_and_services/atmospheres_data/MAVEN/ngims.html](https://pds-atmospheres.nmsu.edu/data_and_services/atmospheres_data/MAVEN/ngims.html)) data are also
 909 available from the PDS. All MAVEN instrument Software Interface Specification (SIS)
 910 documents can be found on the before-mentioned PDS websites. The ATMOCIAAD (Atomic and
 911 Molecular Cross section for Ionization and Aurora Database) database used in the Aeroplanets
 912 model (Gronoff *et al.*, 2021) is available at <https://doi.org/10.5281/zenodo.4632426>.

913 We would like to thank our collaborators on the MAVEN and IUVS Teams, especially
 914 Meredith Elrod and Robin Ramstad, for their contributions in understanding the local Mars
 915 environment during the time period of interest.

916

917 **References**

- 918 Anderson, D. E., and Hord, C. W. (1971). Mariner 6 and 7 Ultraviolet Spectrometer Experiment:
 919 Analysis of hydrogen Lyman-alpha data, *J. Geophys. Res.*, 76 (28), 6666– 6673,
 920 doi:10.1029/JA076i028p06666.
- 921 Bertaux, J.-L., Leblanc, F., Witasse, O., Quemerais, E., Lilensten, J., Stern, S. A., ... Korablev,
 922 O. (2005), Discovery of an aurora on Mar, *Nature*, 435(7043), 790–794, doi:
 923 10.1038/nature03603.
- 924 Bisikalo D.V., Shematovich V.I., Gérard J.-C., Hubert B. (2018), Monte Carlo simulations of the
 925 interaction of fast proton and hydrogen atoms with the Martian atmosphere and
 926 comparison with in situ measurements, *Journal of Geophysical Research: Space Physics*,
 927 V. 123, Issue 7, pp. 5850-5861.

- 928 Chaffin, M. S., J.-Y. Chaufray, I. Stewart, F. Montmessin, N. M. Schneider, and J.-L. Bertaux
929 (2014), Unexpected variability of Martian hydrogen escape, *Geophysical Research*
930 *Letters*, 41(2), 314-320, doi:10.1002/2013gl058578.
- 931 Chaffin, M.S., Kass, D.M., Aoki, S. et al. Martian water loss to space enhanced by regional dust
932 storms. *Nat Astron* 5, 1036–1042 (2021). <https://doi.org/10.1038/s41550-021-01425-w>
- 933 Clarke, J. T., J. L. Bertaux, J. Y. Chaufray, G. R. Gladstone, E. Quémerais, J. Wilson, and D.
934 Bhattacharyya (2014), A rapid decrease of the hydrogen corona of Mars, *Geophysical*
935 *Research Letters*, 41(22), 8013-8020.
- 936 Deighan, J, S. K. Jain, M. S. Chaffin, X. Fang, J. S. Halekas, J. T. Clarke, N. M. Schneider, A. I.
937 F. Stewart, J.-Y. Chaufray, J. S. Evans, M. H. Stevens, M. Mayyasi, A. Stiepen, M.
938 Crismani, W. E. McClintock, G. M. Holsclaw, D. Y. Lo, F. Montmessin, F. Lefevre, B.
939 M. Jakosky (2018), Discovery of Proton Aurora at Mars, *Nature Astronomy*, 2(10), 802.
- 940 England, S. L., Liu, G., Withers, P., Yiğit, E., Lo, D., Jain, S., ... and Elrod, M., (2016),
941 Simultaneous observations of atmospheric tides from combined in situ and remote
942 observations at Mars from the MAVEN spacecraft, *J. Geophys. Res.: Planets*, Volume
943 121, Issue 4, pp. 594-607.
- 944 Galand, M., J. Lilensten, W. Kofman, and R. B. Sidje (1997), Proton transport model in the
945 ionosphere 1. Multistream approach of the transport equations, *Journal of Geophysical*
946 *Research*, 102, 22261–72, <https://doi.org/10.1029/97JA01903>.
- 947 Galand, M., J. Lilensten, W. Kofman, and D. Lummerzheim (1998), Proton transport model in
948 the ionosphere. 2. Influence of magnetic mirroring and collisions on the angular
949 redistribution in a proton beam, *Annales Geophysicae*, 16, 1308–21,
950 <https://doi.org/10.1007/s00585-998-1308-y>.
- 951 Gérard J.-C., Hubert B., Bisikalo D.V., and Shematovich V.I. (2000), Lyman-alpha emission in
952 the proton aurora. *J. Geophys. Res.*, V. 105, No. A7, 15795.
- 953 Gérard, J. C., B. Hubert, B. Ritter, V. I. Shematovich, D. V. Bisikalo (2019), Lyman- α emission
954 in the Martian proton aurora: Line profile and role of horizontal induced magnetic field,
955 *Icarus*, 321, 266-271.
- 956 Girazian and Halekas (2021), Precipitating Solar Wind Hydrogen at Mars: Improved
957 Calculations of the Backscatter and Albedo with MAVEN Observations, *J. Geophys.*
958 *Res.: Planets*, Volume 126, Issue 2, doi: 10.1029/2020JE006666.
- 959 Gronoff, G., C. Simon Wedlund, C. J. Mertens, and R. J. Lillis (2012a), “Computing
960 uncertainties in ionosphere-airglow models: I. Electron flux and species production
961 uncertainties for Mars”, *Journal of Geophysical Research: Space Physics*, 117 (April):
962 4306, 18 PP., <https://doi.org/10.1029/2011JA016930>.
- 963 Gronoff, G., C. Simon Wedlund, C. J. Mertens, M. Barthélemy, R. J. Lillis, and O. Witasse
964 (2012b), “Computing Uncertainties in Ionosphere-Airglow Models: II. The Martian
965 Airglow”, *J. Geophys. Res.* 117 (May): 17 PP.
966 <https://doi.org/10.1029/2011JA017308>.
- 967 Gronoff, G., B. Hegyi, C. Simon Wedlund, & J. Lilensten. (2021), “The ATMOCIAAD database”,
968 *Zenodo*. <https://doi.org/10.5281/zenodo.4632426>

- 969 Halekas, J. S., E. R. Taylor, G. Dalton, G. Johnson, D. W. Curtis, J. P. McFadden, D. L.
 970 Mitchell, R. P. Lin, B. M. Jakosky (2013), The Solar Wind Ion Analyzer for MAVEN,
 971 *Space Science Rev.*, 195(1-4), 125-151.
- 972 Halekas, J. S., Lillis, R. J., Mitchell, D. L., Cravens, T. E., Mazelle, C., Connerney, J. E. P., ... &
 973 Luhmann, J. G. (2015), MAVEN observations of solar wind hydrogen deposition in the
 974 atmosphere of Mars, *Geophys. Res. Lett.*, 42, 8901–8909, doi: 10.1002/2015GL064693.
- 975 Halekas, J. S. (2017), Seasonal variability of the hydrogen exosphere of Mars, *J. Geophys. Res.:*
 976 *Planets*, 122, 901–911, doi: 10.1002/2017JE005306.
- 977 Henderson, S., Halekas, J., Girazian, Z., Espley, J., & Elrod, M. (2022), Influence of magnetic
 978 fields on precipitating solar wind hydrogen at Mars, *Geophysical Research Letters*, 49,
 979 e2022GL099114. <https://doi.org/10.1029/2022GL099114>.
- 980 Huestis, D.L., and J. Berkowitz, (2010). Critical evaluation of the photoabsorption cross section
 981 of CO₂ from 0.125 to 201.6 nm at room temperature, *Advances in Geosciences* Vol. 25:
 982 Planetary Science 229-242
- 983 Hughes, A., Chaffin, M., Mierkiewicz, E., Deighan, J., Jain, S., Schneider, N., (2019), Proton
 984 aurora on Mars: A dayside phenomenon pervasive in southern summer, *J. Geophys. Res.:*
 985 *Space Physics*, 124, 10,533–10,548, doi: 10.1029/2019JA027140.
- 986 Hunten, D.M., F.E. Roach, and J.W. Chamberlain, (1956). A photometric unit for the airglow
 987 and aurora, *Journal of Atmospheric and Terrestrial Physics*, Volume 8, Issue 6, Pages
 988 345-346, [https://doi.org/10.1016/0021-9169\(56\)90111-8](https://doi.org/10.1016/0021-9169(56)90111-8).
- 989 Jakosky, B. M., Lin, R. P., Grebowsky, J. M., Luhmann, J. G., Mitchell, D. F., Beutelschies, G.,
 990 ... & Baker, D. (2015), The Mars atmosphere and volatile evolution (MAVEN) mission,
 991 *Space Sci. Rev.*, 195(1-4), 3-48.
- 992 Jolitz, R. D., C. F. Dong, C. O. Lee, R. J. Lillis, D. A. Brain, S. M. Curry, S. Bougher, C. D.
 993 Parkinson, and B. M. Jakosky (2017), A Monte Carlo model of crustal field influences on
 994 solar energetic particle precipitation into the Martian atmosphere, *J. Geophys. Res. Space*
 995 *Physics*, 122, 5653–5669, doi:10.1002/2016JA023781.
- 996 Jolitz, R. D., Dong, C. F., Rahmati, A., Brain, D. A., Lee, C. O., Lillis, R. J., Curry, and B. M.
 997 Jakosky (2021), Test particle model predictions of SEP electron transport and
 998 precipitation at Mars, *Journal of Geophysical Research: Space Physics*, 126,
 999 e2021JA029132, <https://doi.org/10.1029/2021JA029132>
- 1000 Kallio, E., and S. Barabash (2000), On the elastic and inelastic collisions between precipitating
 1001 energetic hydrogen atoms and Martian atmospheric neutrals [J. Geophys. Res., 105,](https://doi.org/10.1029/2000JA002003)
 1002 [24,973-24,996.](https://doi.org/10.1029/2000JA002003)
- 1003 Kallio, E., & Barabash, S. (2001), Atmospheric effects of precipitating energetic hydrogen atoms
 1004 on the Martian atmosphere, *J. Geophys. Res.:* *Space Physics*, 106(A1), 165-177, doi:
 1005 10.1029/2000JA002003.
- 1006 Lo, D. Y., Yelle, R. V., Schneider, N. M., Jain, S. K., Stewart, A. I. F., England, S. L., ... &
 1007 Chaffin, M. S. (2015), Nonmigrating tides in the Martian atmosphere as observed by
 1008 MAVEN IUVS, *Geophys. Res. Lett.*, 42(21), 9057-9063.

- 1009 Mahaffy, P.R., Benna, M., King, T. *et al.* The Neutral Gas and Ion Mass Spectrometer on the
1010 Mars Atmosphere and Volatile Evolution Mission. *Space Sci Rev* **195**, 49–73 (2015).
1011 <https://doi.org/10.1007/s11214-014-0091-1>
- 1012 McClintock, W. E., N. M. Schneider, G. M. Holsclaw, J. T. Clarke, A. C. Hoskins, I. Stewart, F.
1013 Montmessin, R. V. Yelle (2015), The Imaging Ultraviolet Spectrograph (IUVS) for the
1014 MAVEN Mission, *Space Sci. Rev.*, doi: 10.1007/s11214-014-0098-7.
- 1015 Ritter, B., J.-C. Gérard, B. Hubert, L. Rodriguez, and F. Montmessin (2018), Observations of the
1016 proton aurora on Mars with SPICAM on board Mars Express, *Geophys. Res. Lett.*, 45.
1017 doi: 10.1002/2017GL076235.
- 1018 Schneider, N. M., J. I. Deighan, S. K. Jain, A. Stiepen, A. I. F. Stewart, D. Larson, D. L.
1019 Mitchell, C. Mazelle, C. O. Lee, and R. J. Lillis (2015), Discovery of diffuse aurora on
1020 Mars, *Science*, 350(6261), aad0313.
- 1021 Shematovich V. I., D. V. Bisikalo, C. Diéval, S. Barabash, G. Stenberg, H. Nilsson, Y. Futaana,
1022 M. Holmstrom, and J.-C. Gérard. (2011), Proton and hydrogen atom transport in the
1023 Martian upper atmosphere with an induced magnetic field, *J. Geophys. Res.*, V. 116,
1024 Issue A11, CiteID A11320.
- 1025 Shematovich V.I., Bisikalo D.V., Gérard J.-C., Hubert B. (2019), Kinetic Monte Carlo model of
1026 the precipitation of high-energy proton and hydrogen atoms into the Martian atmosphere
1027 with taking into account the measured magnetic field, *Astronomy Reports*, Vol. 63, No.
1028 10, pp. 835–845.
- 1029 Simon, Cyril. (2006), “Contribution à L’étude Des Entrées d’énergie Solaire Dans L’ionosphère:
1030 Ions Doublement Chargés et Transport Cinétique Des Protons - Application à La Terre et
1031 à Titan.” PhD thesis, Université Joseph-Fourier - Grenoble I. [http://tel.archives-](http://tel.archives-ouvertes.fr/tel-00109802)
1032 [ouvertes.fr/tel-00109802](http://tel.archives-ouvertes.fr/tel-00109802).
- 1033 Simon, C., J. Lilensten, J. Moen, J. M. Holmes, Y. Ogawa, K. Oksavik, and W. F. Denig (2007),
1034 “TRANS4: a new coupled electron/proton transport code - comparison to observations
1035 above Svalbard using ESR, DMSP and optical measurements.” *Annales Geophysicae* 25
1036 (March): 661–73. <https://doi.org/10.5194/angeo-25-661-2007>.
- 1037 Simon Wedlund, C., G. Gronoff, J. Lilensten, H. Ménager, and M. Barthélemy (2011),
1038 “Comprehensive calculation of the energy per ion pair or W values for five major
1039 planetary upper atmospheres.” *Annales Geophysicae* 29 (January): 187–95.
1040 <https://doi.org/10.5194/angeo-29-187-2011>.
- 1041 Stone, S. W., Yelle, R. V., Benna, M., Elrod, M. K., & Mahaffy, P. R. (2018), Thermal structure
1042 of the Martian upper atmosphere from MAVEN NGIMS. *Journal of Geophysical Research: Planets*, 123,
1043 2842–2867. <https://doi.org/10.1029/2018JE005559>.



JGR: Space Physics

Supporting Information for

**Advancing our Understanding of Martian Proton Aurora through a
Coordinated Multi-Model Comparison Campaign**

**Andréa C. G. Hughes^{1,2,3}, Michael Chaffin⁴, Edwin Mierkiewicz³, Justin Deighan⁴,
Rebecca D. Jolitz⁴, Esa Kallio⁵, Guillaume Gronoff^{6,7}, Valery Shematovich⁸, Dmitry
Bisikalo^{8,9}, Jasper Halekas¹⁰, Cyril Simon Wedlund¹¹, Nicholas Schneider⁴, Birgit
Ritter^{12,13}, Zachary Girazian¹⁰, Sonal Jain⁴, Jean-Claude Gérard¹², and Bradley
Hegy^{6,7}**

¹ NASA Goddard Space Flight Center, Greenbelt, MD, United States.

² Department of Physics & Astronomy, Howard University, Washington, DC, United States.

³ Center for Space and Atmospheric Research (CSAR) and the Department of Physical Sciences, Embry-Riddle Aeronautical University, Daytona Beach, Florida, United States.

⁴ Laboratory for Atmospheric and Space Physics, University of Colorado, Boulder, CO, USA. United States.

⁵ Aalto University, School of Electrical Engineering, Department of Electronics and Nanoengineering, Espoo, Finland.

⁶ NASA Langley Research Center, Hampton, VA, United States.

⁷ Science Systems and Application Inc. Hampton, VA, United States.

⁸ Institute of Astronomy of the Russian Academy of Sciences, Moscow, Russia.

⁹ National Center for Physics and Mathematics, Russian Federation, Moscow, Russia.

¹⁰ Department of Physics and Astronomy, University of Iowa, Iowa City, IA, United States.

¹¹ Space Research Institute, Austrian Academy of Sciences, Graz, Austria.

¹² Royal Observatory of Belgium, Brussels, Belgium.

¹³ Université de Liège, LPAP – STAR Institute, Liege, Belgium.

Contents of this file

Text S1 to S4

Figures S1 to S4

Tables S1 to S1

36

37 **Introduction**

38 Herein we provide supplemental materials regarding the models used in the study,
39 cross sections used in the models, and additional information regarding the
40 locations of MAVEN and MAVEN/IUVS for observations taken during the orbit of
41 interest. In the Supplementary Text section, we present detailed descriptions of
42 each of the four proton/hydrogen precipitation models used in the study.
43 Descriptions are written by each modeling team and appropriate references are
44 given at the end of each section. In the Supplementary Figures section, we present
45 S1) maps showing the locations of the MAVEN spacecraft during the orbit used in
46 this study (including comparative locations of strong crustal fields), S2) ephemeris
47 data for the MAVEN/IUVS instrument while acquiring the periapsis limb scan data
48 used in this study, S3) relevant profiles used for the coronal thermal H background
49 subtraction method described in the text, and S4) preliminary results comparing the
50 assumption of monodirectional incident particle movement versus isotropic. Lastly,
51 we include a Supplementary Table with details regarding cross sections used by
52 each model and relevant references.

53

54 **Text S1.**

55 **Kallio 3-D Monte Carlo Model Description**

56 *(i) General introduction: nature of the model, brief history of its development, and*
57 *general references*

58 The Kallio model is described in detail in *Kallio and Barabash, 2000* and *2001*.
59 The model is a 3-D Monte Carlo (MC) model where the incident particle, either H⁺ or H,
60 collides with neutral particles after which the velocity of the particle is changed. The
61 model contains 6 elastic and 24 inelastic processes but, in this study, only the processes
62 mentioned in the main text of this paper were used.

63 The model uses a Cartesian coordinate system both for the positions and velocities
64 of the precipitating particles. In the coordinate system the x-axis points from the center of
65 Mars toward the Sun.

66

67 *(ii) Inputs, processes included (with relevant cross section references), and outputs*

68 The model inputs are neutral atom densities, energy dependent total cross-sections
69 (CS), the differential scattering cross-sections (DSCS), the number of precipitating
70 particles (N_H), and the initial positions ($\mathbf{r}_{\text{particle}}(t=0)$) and velocities ($\mathbf{v}_{\text{particle}}(t=0)$) of the
71 precipitating particles -- in the present case hydrogen atoms (H).

72 The total cross sections are given in *Kallio and Barabash, 2001* (Table 1 and Fig.
73 3) and the DSCS scattering angle distribution in *Kallio and Barabash, 2000* (Fig. 1,
74 “nominal”) and *2001* (Fig. 2). Total cross sections give the probability that a collision

75 occurs. Random numbers are used to model if a collision occurs, and which collision
 76 process occurs. If a collision happens, then the DSCS determines the new velocity of the
 77 incident particle after collision. The value of the scattering angle is obtained by using a
 78 new random variable.

79

80 *(iii) Implementation and technical aspects: assumptions and constraints, domain of*
 81 *applicability and grid description, spatial resolution and timesteps, number of particles,*
 82 *overall performance, etc.*

83 In the simulation, particles are injected into the upper atmosphere at the point $[x, y,$
 84 $z] = [260 \text{ km} + R_{\text{Mars}}, 0, 0]$, where the radius of the Mars, R_{Mars} , was in the simulation
 85 3393 km. The velocity of the particles in the analysis presented in this paper was a
 86 constant $\mathbf{v} = [v_x, v_y, v_z] = [-400, 0, 0]$ km/s, i.e., a beam of particles initially moving
 87 exactly along the Sun-Mars line.

88 The model saves the position and the velocity of the particle if it has a Ly- α
 89 collision process. The Ly- α volume production rate was derived from the saved positions
 90 of Ly- α processes by collecting the number of the Ly- α collision processes ($d\#_k^{\text{hf}}$) at a
 91 given altitude (h) range: $dh_k \equiv h_{k+1} - h_k$. Then in Step 1 runs the Ly- α volume of the
 92 emission was derived by using a 1-D approximation, i.e., assuming that the area of the
 93 emission perpendicular to the x-axis (dA_{hf}) is equal to the initial area in the solar wind
 94 (dA_{sw}) through which the precipitating particles initially came, $dA_{\text{hf}} = dA_{\text{sw}}$. Note that the
 95 inaccuracy caused by the 1-D approximation, $dA_{\text{hf}} = dA_{\text{sw}}$, is small because the horizontal
 96 movement of the colliding particles in the atmosphere is small compared with the radius
 97 of the planet. Therefore, the volume (dV_k) from which the emission came within dh_k in
 98 Step 1 runs was assumed to be $dV_k = dh_k \times dA_{\text{sw}}$. In Step 2 runs the volume dV_k was
 99 derived without any approximations from the space angle and the altitude range.

100 The altitude dependent Ly- α volume emission rate

$$101 \quad q_k^{\text{hf}} = d\#_k^{\text{hf}} / (dt \times dV_k) = d\#_k^{\text{hf}} / (dt \times dh_k \times dA_{\text{hf}}), \quad (1)$$

102 which, as mentioned above, was in Step 1 runs derived by approximating $dA_{\text{hf}} = dA_{\text{sw}}$

$$103 \quad q_k^{\text{hf}} = d\#_k^{\text{hf}} / (dt \times dh_k \times dA_{\text{sw}}), \quad (2)$$

104 is finally obtained from the particle flux of the precipitating H particles (j_{H}), the number
 105 of the particles used in the MC simulation (N_{H}) and the time (dt) which takes N_{H} particles
 106 to go through the area dA_{sw} : $N_{\text{H}} = j_{\text{H}} dt \times dA_{\text{sw}}$. This gives $dt \times dA_{\text{sw}} = N_{\text{H}} / j_{\text{H}}$ and Eq (2)
 107 gets the form

$$108 \quad q_k^{\text{hf}} = d\#_k^{\text{hf}} / (dt \times dV_k) = j_{\text{H}} [d\#_k^{\text{hf}} / (dh_k \times N_{\text{H}})]. \quad (3)$$

109 In the analyzed simulation N_{H} was 5000 and 100,000 in Step 1 and Step 2 runs,
 110 respectively. As can be seen in Eq. (3) the particle flux j_{H} is just a scaling factor and in
 111 this paper, it was $10^7 \text{ cm}^{-3} \text{ s}^{-1}$. In the plots presented in this paper the Ly- α emission
 112 altitude profiles were derived in 1 km altitude bins, i.e., $dh_k = 1 \text{ km}$. This provided a
 113 relatively good compromise between modest statistical fluctuations and the accurate
 114 determination of the peak emission value and altitude.

115

116 *(iv) Strengths and applications most suited for the model*

117 The largest uncertainty for the obtained Ly- α volume emission rate q_k^{hf} is related to
 118 the uncertainty of the total cross-sections used and the differential scattering cross
 119 sections between H and H^+ particles and CO_2 molecules. In the simulation many of these

120 H/H⁺ collisions with CO₂ are modeled with H/H⁺ collisions with O₂ and N₂ which was
121 published in the literature (see *Kallio and Barabash*, 2001, Table 1, for details).

122 As described in *Kallio and Barabash*, 2000 and 2001, functional forms of the
123 adopted DSCS are modeled following *Noël and Prölss* (1993). The used DSCS (see
124 *Kallio and Barabash*, 2000, Fig. 1a, the “nominal” DCSC and *Kallio and Barabash*,
125 2001, Fig. 2) is a fit to the data of H – O₂ collisions from *Newmann et al.*, 1986, Table 4.

126

127 It is worth noting that although the statistical fluctuations in the derived emission
128 altitude profiles could be reduced by using a larger number of precipitating particles in
129 the 1 km altitude binning used, the statistical fluctuations are relatively modest already
130 for the number of particles used.

131 It is also worth noting that the MC model used can be automatically used in future
132 more complicated situations than done in this paper. In this study the precipitating
133 particles formed a monoenergetic beam. However, the velocity distribution function can
134 be more complicated; for example, a Maxwellian velocity distribution function, or the
135 velocities can be read from a file. Moreover, the atmospheric density profile, $n(\mathbf{r})$ can be
136 2-D, say $n(\mathbf{r}) = n(\text{SZA}, h)$. In such a case the MC model can be used to derive altitude
137 profiles at a given SZA (see *Kallio and Barabash*, 2001, for details). The atmospheric
138 density can also be 3-D, i.e., $n(\mathbf{r}) = n(x, y, z)$, which would result in the 3-D Ly- α
139 emission rates. In the simulation the particle flux and their velocity distribution can also
140 have latitude-longitude dependence (see *Kallio and Janhunen*, 2001, for details).

141

142 References:

143 Kallio, E., and S. Barabash, On the elastic and inelastic collisions between precipitating
144 energetic hydrogen atoms and Martian atmospheric neutrals [J. Geophys. Res.,](#)
145 [105, 24,973-24,996](#), 2000.

146 Kallio, E., and S. Barabash, Atmospheric effects of precipitating energetic hydrogen
147 atoms on the Martian atmosphere, [J. Geophys. Res., 106, 165-178](#), 2001.

148 Kallio, E., and P. Janhunen, Atmospheric effects of proton precipitation in the Martian
149 atmosphere and its connection to the Mars-solar wind interaction, [J. Geophys.](#)
150 [Res., 106, 5617-5634](#), 2001.

151 Newman, J. H., Y. S. Chen, K. A. Smith and R. F. Stebbings, Differential cross sections
152 for scattering of 0.5-, 1.5-, and 5.0-keV hydrogen atoms by He, H₂, N₂, and O₂,
153 [J. Geophys. Res., Volume 91, Issue A8, Pages 8947-8954](#), 1986.

154 Noël, S. and G. W. Prölss, Heating and radiation production by neutralized ring current
155 particles. [J. Geophys. Res., Volume 98, Issue A10, Pages 17317-17325](#), 1993.

156 Rees, M. H., *Physics and Chemistry of the Upper Atmosphere*, Cambridge Univ. Press,
157 New York, 1989.

158 Rudd, M. E., Kim, Y. K., Madison, D. H., & Gallagher, J. W., Electron production in
159 proton collisions: Total cross sections. *Reviews of Modern Physics*, 57, 965– 994,
160 1985.

161 Van Zyl, B., Neumann, H., Le, T. Q., and R.C. Amme, H + N₂ and H + O₂ collisions:
162 Experimental charge-production cross sections and differential scattering
163 calculations, *Phys. Rev. A* 18(2):506-516, 1978.

164 Van Zyl, B., and H. Neumann, Lyman α emission cross sections for low-energy H and
165 H+ collisions with N₂ and O₂, *J. Geophys. Res.*, 93(A2):1023-1027, 1988.
166

167 **Text S2.**

168 **Jolitz 3-D Monte Carlo Model Description (Name: “ASPEN”)**

169 ASPEN (Atmospheric Scattering of Protons, Electrons, and Neutrals) is a 3-D
170 Monte Carlo test particle simulation. This model was initially developed to predict
171 atmospheric ionization rates at Mars by solar energetic particles, which have higher
172 energies than the ENAs studied in this paper [Jolitz *et al.*, 2017] and has since been used
173 to predict precipitating SEP electron fluxes at Mars [Jolitz *et al.*, 2021]. The simulation
174 solves the Lorentz force equations for energetic particle motion and uses a Monte Carlo
175 approach to predict collisions and resulting energy loss in the atmosphere. Since
176 magnetic fields were set to zero for this study, the transport equations reduced to ballistic
177 motion.

178 The collisional energy degradation algorithm used in ASPEN was originally
179 developed and described in Lillis *et al.* [2008] for an electron precipitation model. It is
180 very similar to the Kallio model in approach. Stochastic collisions were modeled by
181 inverting the relation between intensity, density, and absorption cross-section for a
182 particle beam incident on a medium of scatterers (colloquially known as Beer’s law) to
183 dynamically calculate a probability distribution function that is combined with a random
184 number to predict variable distances between collisions. This probability distribution
185 function is calculated for each individual particle and depends on the position, path, and
186 energy through the planetary atmosphere. Similarly, whenever a collision occurs, the type
187 of collision is predicted probabilistically using the relative cross-section of each possible
188 collisional process and the particle energy is decremented by the corresponding energy
189 loss. As a particle loses energy, the relative cross-sections of each process change. For
190 example, a 2 keV proton colliding with a carbon dioxide molecule has a roughly 70%
191 likelihood of capturing an electron, but the likelihood for the same process when the
192 proton is 20 eV is only 20%.

193 This model is highly dependent on the choice of cross-sections. For the
194 application in this study, the selected cross-sections for hydrogen and proton impact on
195 carbon dioxide are described in Jolitz *et al.* [2017], with one exception. The cross-
196 sections for proton- and hydrogen-impact excitation was replaced with Lyman-alpha
197 emission cross-sections. Unfortunately, experimental measurements of the Lyman-alpha
198 emission cross-section from proton and hydrogen atom impact on carbon dioxide is
199 limited. As of the time of this paper’s writing, only one set of measurements exist for
200 1-25 keV protons and hydrogen atoms [Birely and McNeal, 1972]. The cross-section for
201 emission by protons and hydrogen atoms below 1 keV is unknown. In order to
202 approximate emission from particles at these energies, ASPEN uses a cross-section
203 calculated by scaling the corresponding emission cross-sections from impact on
204 molecular oxygen. ASPEN also accounts for the fact that proton-induced Lyman-alpha

205 emission can only occur in addition to a charge exchange collision, since Lyman-alpha
206 can only be emitted by a hydrogen atom.

207 Since ASPEN is a 3-D Monte Carlo simulation, predicting an accurate emission
208 rate requires appropriate choice of initial conditions and a large volume of simulated
209 particles. For Step 1, we simulated 10,000 particles incident on the subsolar point from an
210 altitude of 600 km and calculated the emission rate by binning all Lyman-alpha emitting
211 collisions as a function of altitude and multiplying by the incident flux. For Step 2, we
212 simulated 10,000 particles uniformly distributed in space on a plane perpendicular to the
213 direction of solar wind flow. Each particle represents a fraction of the assumed incident
214 flux. The emission rate was then calculated by weighing the total number of emissions
215 binned by altitude, solar zenith angle, and the fraction of flux associated with each
216 simulated particle.

217

218 References:

219 Avakyan, S. V., R. N. Il'in, V. M. Lavrov, and G. N. Ogurtsiv (1998), *Collision Processes*
220 *and Excitation of UV Emission From Planetary Atmospheric Gases: A Handbook*
221 *of Cross Sections*, Gordon and Breach, Amsterdam.

222 Barnett, C. F., Ray J. A., Ricci, E., Wilkers, M. I., et al. 1977. *Atomic data for controlled*
223 *fusion research*. Report no. ORNL-5296. Oak Ridge, TN: Oak Ridge National
224 *Laboratory*.

225 Birely, J.H., and R.J. McNeal (1972), Lyman-alpha emission cross sections for collisions
226 of 1-25 keV H+ and H with CO, CO₂, CH₄, and NH₃, *J.Chem Phys.*, 56 (5),
227 2189-94, doi:10.1063/1.1677518.

228 Jolitz, R. D., C. F. Dong, C. O. Lee, R. J. Lillis, D. A. Brain, S. M. Curry, S. Bougher, C.
229 D. Parkinson, and B. M. Jakosky (2017), A Monte Carlo model of crustal field
230 influences on solar energetic particle precipitation into the Martian atmosphere, *J.*
231 *Geophys. Res. Space Physics*, 122, 5653–5669, doi:10.1002/2016JA023781.

232 Jolitz, R. D., Dong, C. F., Rahmati, A., Brain, D. A., Lee, C. O., Lillis, R. J., Curry, and
233 B. M. Jakosky (2021). Test particle model predictions of SEP electron transport
234 and precipitation at Mars. *Journal of Geophysical Research: Space Physics*, 126,
235 e2021JA029132. <https://doi.org/10.1029/2021JA029132>

236 Lillis, R. J., D. L. Mitchell, R. P. Lin, and M. H. Acuña (2008), Electron reflectometry in
237 the Martian atmosphere, *Icarus*, 194(2) 544-61, doi:10.1016/j.icarus.2007.09.030.

238 McNeal, R.J. (1970), Production of positive ions and electrons in collisions of 1-25-keV
239 protons and hydrogen atoms with CO, CO₂, CH₄, and NH₃, *J. Chem. Phys.* 53,
240 4308.

241 Nakai, Y., T. Shirai, T. Tabata, and R. Ito (1987), Cross sections for charge transfer of
242 hydrogen atoms and ions colliding with gaseous atoms and molecules, *At. Data*
243 *Nucl. Data Tables*, 37, 69– 101, doi:10.1016/0092-640X(87)90005-2.

244 Newman, J. H., Chen, Y.S., Smith, K.A., and R.F. Stebbings (1986), Differential cross
245 sections for scattering of 0.5-, 1.5-, and 5.0-keV hydrogen atoms by He, H₂, N₂,
246 and O₂, *J. Geophys. Res.* 91(A8), 8947–8954.

- 247 Noël S., and G. W. Prölss (1993), Heating and radiation production by neutralized ring
 248 current particles. *J Geophys Res* 98:17317–17325.
- 249 Rudd, M. E., Kim, Y. K., Madison, D. H., & Gallagher, J. W. (1985), Electron
 250 production in proton collisions: Total cross sections. *Reviews of Modern Physics*,
 251 57, 965– 994.
- 252 Van Zyl, B., Neumann, H., Le, T. Q., and R.C. Amme (1978), H + N₂ and H + O₂
 253 collisions: Experimental charge-production cross sections and differential
 254 scattering calculations, *Phys. Rev. A* 18(2):506-516.
- 255 Van Zyl, B., and H. Neumann (1988), Lyman α emission cross sections for low-energy H
 256 and H⁺ collisions with N₂ and O₂, *J. Geophys. Res*, 93(A2):1023-1027.
 257

258 **Text S3.**

259 **Bisikalo/Shematovich *et al.* 1-D Monte Carlo Model Description**

260 The Bisikalo/Shematovich *et al.* model is a 1-D kinetic Monte Carlo model. The
 261 model considers three primary processes: 1) precipitation of high-energy hydrogen atoms
 262 and protons that lose their kinetic energy in the elastic and inelastic collisions, 2)
 263 ionization of target atmospheric molecules/atoms, and 3) charge transfer and electron
 264 capture collisions with the major atmospheric constituents (i.e., CO₂, N₂, and O).
 265 Secondary fast hydrogen atoms and protons carry enough kinetic energy to cycle through
 266 the collisional channels mentioned above and result in a growing set of translationally
 267 and internally excited atmospheric atoms and/or molecules.
 268 To study the precipitation of high-energy H/H⁺ flux into the planetary atmosphere, we
 269 solve the kinetic Boltzmann equations (Shematovich *et al.*, 2011) for H⁺ and H, including
 270 the collision term:

$$\mathbf{v} \frac{\partial}{\partial \mathbf{r}} f_{H/H^+} + \left(\mathbf{g} + \frac{e}{m_{H^+}} \mathbf{v} \times \mathbf{B} \right) \frac{\partial}{\partial \mathbf{v}} f_{H/H^+} = Q_{H/H^+}(\mathbf{v}) + \sum_{M=O, N_2, CO_2} J_{mt}(f_{H/H^+}, f_M). \quad (1)$$

271 Equation (1) is written in the standard form for the velocity distribution functions
 272 $f_{H/H^+}(r,v)$, and $f_M(r,v)$ for hydrogen atoms and protons (Gérard *et al.*, 2000). The source
 273 term Q_{H/H^+} describes the production rate of secondary H/H^+ particles and the elastic
 274 and inelastic collisional terms J_{mt} for H/H^+ describe the energy and momentum transfer to
 275 the ambient atmospheric gas which is characterized by local Maxwellian velocity
 276 distribution functions. Our kinetic Monte Carlo model (Gérard *et al.*, 2000; Shematovich
 277 *et al.*, 2011) is used to solve kinetic equation (1). The model is 1-D in geometric space
 278 and 3-D in velocity space. Nevertheless, the 3-D trajectories of H/H^+ are calculated in the
 279 code with final projection on radial direction. In the current version of the MC model
 280 (Shematovich *et al.*, 2019) an arbitrary structure of the induced magnetic field of Mars is
 281 included; that is, all three components of the magnetic field $\mathbf{B} = \{B_x, B_y, B_z\}$, were taken
 282 into account. The details of the model implementation and statistics control with the
 283 variance below 10% can be found in (Shematovich *et al.*, 2019).

284
 285 The essence of the kinetic Monte Carlo model is accounting of all possible
 286 collisions in the atmospheric region studied. Therefore, statistics for all collisional
 287 processes are accumulated during the numerical realization of the kinetic model of the
 288 proton aurora. It provides a good basis for the evaluation of the Ly- α source functions as
 289 keeping of all excitation processes and their spatial characteristics makes it possible to
 290 determine the statistical distribution of the emitted Ly- α photons.

291 The energy deposition rate of H/H^+ flux is determined by the cross sections of the
 292 collisions with the ambient gas. The energy lost by the H/H^+ in a collision is determined
 293 by the scattering angle χ

294
$$\Delta E \sim E \times (1 - \cos\chi),$$

295 where E is the initial energy of the impacting proton or hydrogen atom. It is apparent that
296 the energy loss for collisions in forward direction (for $\chi < 90^\circ$) at small scattering angles
297 χ is less than that for larger scattering angles. A key aspect of this kinetic MC model is
298 the probabilistic treatment of the scattering angle distribution, which influences both the
299 energy degradation rate and the angular redistribution of the precipitating protons and
300 hydrogen atoms (Bisikalo et al., 2018; Shematovich et al., 2019). The kinetic model
301 utilizes both total and differential cross sections when calculating the post-collision
302 velocities for high-energy precipitating H/H⁺ and atmospheric particles. In the model, the
303 most recent measurements or calculations of the required cross sections were adopted.
304 The cross sections and scattering angle distributions for H/H⁺ collisions with CO₂ are
305 taken from Nakai et al. (1987) for charge exchange and stripping collisions, from Haider
306 et al. (2002) for ionization, Lyman alpha and Balmer alpha excitation, and from Lindsay
307 et al. (2005) for scattering angle distributions. The elastic and other inelastic collisions
308 cross sections for H/H⁺ collisions with CO₂ are assumed to be the same as for O₂ (see,
309 for details, Gérard et al. (2000)). The region under study is limited by the lower
310 boundary, which is placed at 80 km, where H/H⁺ particles are efficiently thermalized. The
311 upper boundary is set at 500 km, where measurements or calculations of the precipitating
312 fluxes of protons or hydrogen atoms are used as a boundary condition. Both table and/or
313 analytic (Maxwellian and/or kappa-distribution) functions representing the energy spectra
314 as well as the pitch-angle (monodirectional, isotropic, or limited by cone) distributions of
315 precipitating particles could be used at the upper boundary. Detailed description of all
316 modeled numerical aspects used for this kinetic MC model study could be found in recent
317 papers (Bisikalo *et al.*, 2018; Shematovich *et al.*, 2019).

318
319 References:

- 320 Gérard J.-C., Hubert B., Bisikalo D.V., and Shematovich V.I. Lyman-alpha emission in
321 the proton aurora. *J. Geophys. Res.*, 2000, V. 105, No. A7, pp. 15795.
- 322 Shematovich V. I., D. V. Bisikalo, C. Diéval, S. Barabash, G. Stenberg, H. Nilsson, Y.
323 Futaana, M. Holmstrom, and J.-C. Gérard. Proton and hydrogen atom transport in
324 the Martian upper atmosphere with an induced magnetic field. *J. Geophys. Res.*,
325 2011, V. 116, Issue A11, CiteID A11320.
- 326 Bisikalo D.V., Shematovich V.I., Gérard J.-C., Hubert B. Monte Carlo simulations of the
327 interaction of fast proton and hydrogen atoms with the Martian atmosphere and
328 comparison with in situ measurements. *Journal of Geophysical Research: Space*
329 *Physics*, 2018, V. 123, Issue 7, pp. 5850-5861.
- 330 Shematovich V.I., Bisikalo D.V., Gérard J.-C., Hubert B. Kinetic Monte Carlo model of
331 the precipitation of high-energy proton and hydrogen atoms into the Martian
332 atmosphere with taking into account the measured magnetic field. *Astronomy*
333 *Reports*, 2019, Vol. 63, No. 10, pp. 835–845.
- 334 Haider, S.A., Seth S. P., Kallio E., and Oyama K.I. Solar EUV and electron-proton-
335 hydrogen atom-produced ionosphere on Mars: Comparative studies of particle
336 fluxes and ion production rates due to different processes, *Icarus*, 2002, V. 159,
337 pp. 18-30.

338 Lindsay, B. G., Yu W. S., and Stebbings R. F. Cross sections for electron capture and
339 loss by keV oxygen atoms in collisions with CO and CO₂, *J. Geophys. Res.*,
340 2005, V. 110, pp. A02302.

341 Nakai, Y., Shirai T., Tabata T., and Ito R. Cross sections for charge transfer of hydrogen
342 atoms and ions colliding with gaseous atoms and molecules, *Atomic Data and*
343 *Nuclear Data Tables*, 1987, V.37, pp. 69-101.

344

345 **Text S4.**

346 **Gronoff *et al.* 1-D Kinetic Model Description (Name: “Aeroplanets”)**

347 *A. Introduction*

348 The *Aeroplanets* model (Gronoff *et al.*, 2012a; Gronoff *et al.*, 2012b; Simon
349 Wedlund *et al.* 2011) is a 1-D kinetic transport model computing the ionization and
350 excitation of atmospheric species by photon, electron, proton, and cosmic ray impacts,
351 including the effect of secondary particles (photoelectrons, secondary electrons and
352 protoelectrons). It is based on the Trans* model series, initially developed for the Earth
353 (Lilensten *et al.*, 1999; Lummerzheim and Lilensten 1994; Simon *et al.*, 2007 as Trans4),
354 and subsequently adapted to Venus (Gronoff *et al.*, 2007, 2008), Mars (Witasse *et al.*,
355 2002, 2003; Simon *et al.*, 2009; Nicholson *et al.*, 2009), Titan (Gronoff, Lilensten, and
356 Modolo 2009; Gronoff *et al.*, 2009a, 2009b), etc., and including several other modules
357 such as a fluid model. *Aeroplanets* constitutes an improvement in modularity and
358 adaptability over Trans4, with every separate module having the option of being turned
359 off to study one specific aspect of particle precipitation in the atmosphere of planets.

360 The proton transport module is based on the work of Galand *et al.* (1997, 1998),
361 Simon (2006) and Simon *et al.* (2007) for Earth, who solved semi-analytically the
362 coupled proton-hydrogen dissipative kinetic transport equation for protons and hydrogen
363 atoms charge-changing with neutral gas M:

364
$$H^+ + M \rightarrow H + M^+ \text{Electron capture, } \sigma_{10} \quad H + M \rightarrow H^+ + M +$$

365
$$e^- \text{Electron loss/stripping, } \sigma_{01}.$$

366 It naturally includes angular redistributions due to magnetic mirror effects and to
367 collisions (Galand *et al.*, 1998)

368

369 *B. Inputs and outputs*

370 Inputs to the *Aeroplanets* model include cross sections, the vertical profile of atmosphere
371 composition (*i.e.*, composition at different altitudes), and the precipitating fluxes of
372 particles such H and H⁺ at the top of the atmosphere. Outputs include the vertical profile
373 of H and H⁺ differential energy fluxes, and the vertical profile of the production rate of
374 excited and ionized species and electrons, including emissions. The produced
375 photoelectrons can be plugged into the main *Aeroplanets* electron model as an external
376 and additional source of ionization in the atmosphere.

377 Cross sections in *Aeroplanets* are taken from the latest version of the
378 ATMOCIAAD cross section and reaction rate database compiled and developed by Simon
379 Wedlund *et al.* (2011), Gronoff *et al.* (2012a) and Gronoff *et al.* (2020), and freely
380 available in Gronoff *et al.* (2021) In ATMOCIAAD, experimental and theoretical cross

381 sections as well as their uncertainties are collected. Many proton-hydrogen impact cross
 382 sections have been discussed in the seminal works of Avakyan *et al.* (1998) and, in a
 383 lesser degree, of Nakai *et al.* (1987); they contain a critical review of processes for
 384 photons, e^- , H, H^+ colliding with various gases of aeronomic interest and have been fully
 385 integrated into ATMOCIAAD.

386 Specifically, the proton transport code uses the following energy-dependent cross
 387 sections, process by process:

- 388 • **Elastic.** Parameterisations of Kozelov and Ivanov (1992) originally valid for (H^+ ,
 389 H) collisions with N_2 , and assumed to be the same for CO_2 because of the lack of
 390 any recent measurements. The parameters are available in their Tables 1 and 2.
- 391 • **Ionization.** For H^+ , Rudd *et al.* (1983) for high energies, extended at $E < 5$ keV by
 392 (Avakyan *et al.*, 1998). For H atoms, cross sections are based on Basu *et al.* (1987)
 393 for N_2 and on Avakyan *et al.* (1998) for the rescaling factor.
- 394 • **Electron capture ($H^+ \rightarrow H$).** Kusakabe *et al.* (2000) for 0.2-4 keV protons, review
 395 by Avakyan *et al.* (1998) based on all other available data for higher energies
 396 (Desesquelles, Do Cao, and Dufay 1966; Barnett and Gilbody 1968; Toburen,
 397 Nakai, and Langley 1968; McNeal 1970; Rudd *et al.*, 1983 for 5 – 150 keV). Note
 398 that recent sub-keV measurements have been made by Werbowy and Pranszke
 399 (2016) for CO and CO_2 , although these are not yet implemented in the
 400 ATMOCIAAD.
- 401 • **Electron loss ($H \rightarrow H^+$).** Smith *et al.*, (1976) between 0.25 – 5 keV, review by
 402 Avakyan *et al.*, (1998) using N_2 σ_{01} cross sections (Green and Peterson 1968) based
 403 on all other available data for higher energies.
- 404 • **Ly- α H($2p$) and H($2s$) states.** For both H^+ and H collisions, exciting state H($2p$)
 405 (Birely and McNeal 1972) corrected by factor 0.9 presumably because of
 406 observation angle issues as per the recommendation of Avakyan *et al.* (1998). For
 407 both impactors creating state H($2s$), factor 1.35 on the measurements of (Birely and
 408 McNeal 1972) is applied.

409 Although ATMOCIAAD is an extensive collection of cross sections, there is still a rather
 410 poor characterization of cross sections at low energies (typically in the sub-keV range).

411

412 Regarding differential cross sections, Aeroplanets uses phase functions that are
 413 convolved with the energy-dependent cross sections above. For the particular cases
 414 computed for Step 1 of the present study, the following is used: for the two charge-
 415 transfer (10 and 01) and elastic cross sections, the screened Rutherford function is used,
 416 equal to that of the electrons with a screening parameter ϵ of 10^{-3} (this is the same as in
 417 Galand *et al.*, 1997, 1998 and Simon 2006, Simon *et al.*, 2007 for Earth's atmosphere):

$$418 \quad \xi(\cos\vartheta) = \frac{4\epsilon(1 + \epsilon)}{(1 + 2\epsilon - \cos\vartheta)^2}$$

419

420 with $\vartheta = \mu\mu' + \sqrt{1 - \mu'^2}\sqrt{1 - \mu^2}\cos(\phi - \phi')$. μ and μ' are the cosine of the pitch
 421 angles before and after the collision, whereas ϕ and ϕ' are the azimuthal angles before
 422 and after the collision. For ionization, forward scattering is assumed following Galand *et*
 423 *al.*, (1998) for the Earth case.

424 Because of the seamless implementation of ATMOCIAAD as input to Aeroplanets,
 425 other available sets of cross sections may be used. It is possible to estimate the

426 uncertainties from the cross sections using a Monte-Carlo approach as described in
427 (Gronoff *et al.*, 2012a; Gronoff *et al.*, 2012b). The outputs of the proton-transport model
428 are the ionization and dissociation rates (including excited states productions), the
429 proton/H induced electron flux (which can be used in the electron model), and the
430 proton/H fluxes at the different altitudes.

431

432 *C. Implementation*

433 The solution of the dissipative coupled Boltzmann H/H⁺ equation is based on the seminal
434 work of Galand *et al.*, (1997, 1998), later developed and adapted as a module into
435 Aeroplanets following Simon *et al.*, (2007). It is based on the idea that dissipative forces
436 responsible for angular redistributions (due to elastic scattering) can be introduced in the
437 force term of the generalized Boltzmann equation (Galand *et al.*, 1997). Rearranging the
438 energy/angle terms of the H⁺/H coupled system of equations leads to a linear system of
439 equations parametrized by a large sparse square matrix *A* containing the energy
440 degradation without angular redistributions of the incoming particle, for each altitude *z*
441 so that:

$$442 \quad \frac{\partial \Phi}{\partial z} = A\Phi + B$$

443 $\Phi = (\phi_{H^+} \ \phi_H)$ is the vector-flux of protons and hydrogen precipitating particles and *B*,
444 the angular degradation term, is thus the term coupling downward and upward fluxes.
445 Moreover, the mirror mode term can be switched on or off depending on the planet's
446 configuration. The equation can be solved by calculating the exponential of matrix *A* for
447 a typical grid of 100 energies and 10 angles, both of which can be increased by the user
448 for better resolution.

449 In order to achieve such a feat of simplification for a complex system of equations, the
450 following assumptions are made in the case of the Mars code: (i) plane parallel geometry,
451 with the atmosphere stratified horizontally, and the pitch angle of the particles can be
452 imposed, (ii) external forces neglected, (iii) steady-state fluxes, (iv) continuous slowing
453 down approximation assumed because of the low energetic losses by the precipitating
454 particles compared to the incident energy of the particles.

455

456 *D. Strengths and applications*

457 Aeroplanets is better qualified for the fast computation of the proton precipitation from a
458 measured spectra near the planet, and for the fast computation of the whole effect of that
459 precipitation thanks to its coupling with a secondary electron transport model. The
460 analytic computation approach and assumed geometry prevent the computation within
461 very complex magnetic topologies (which are best handled by Monte-Carlo models) but
462 is well suited for handling large sets of initial angles and energies.

463

464 References:

465 Avakyan, S.V., R.N. Li'In, V.M. Lavrov, and G.N. Ogurtsov. 1998. Collision processes
466 and excitation of UV emission from planetary atmospheric gases: a handbook of
467 cross sections. Taylor & Francis, Amsterdam.

468 Barnett, C. F., and H. B. Gilbody. 1968. "Measurements of Atomic Cross Sections in
469 Static Gases." In Atomic Interactions Part a, edited by Benjamin Bederson and
470 Wade L. Fite, 7:390.

- 471 Basu, B., J. R. Jasperse, R. M. Robinson, R. R. Vondrak, and D. S. Evans. 1987. "Linear
472 transport theory of auroral proton precipitation: A comparison with observations."
473 J. Geophys. Res. 92 (A6): 5920–32. <https://doi.org/10.1029/JA092iA06p05920>.
- 474 Birely, J. H., and R. J. McNeal. 1972. "Lyman-Alpha Emission Cross Sections for
475 Collisions of 1-25 keV H⁺ and H with CO, CO₂, CH₄, and NH₃." J. Chem. Phys.
476 56 (5): 2189–94. <https://doi.org/10.1063/1.1677518>.
- 477 Desesquelles, J., G. Do Cao, and M. Dufay. 1966. "Etude de l'ionisation de quelques gaz
478 par des ions accélérés H⁺ et H₂⁺." C. R. Acad. Sci. Paris 262 (B): 1329–32.
- 479 Galand, M., J. Lilensten, W. Kofman, and D. Lummerzheim. 1998. "Proton transport
480 model in the ionosphere. 2. Influence of magnetic mirroring and collisions on the
481 angular redistribution in a proton beam." Annales Geophysicae 16 (October):
482 1308–21. <https://doi.org/10.1007/s00585-998-1308-y>.
- 483 Galand, M., J. Lilensten, W. Kofman, and R. B. Sidje. 1997. "Proton transport model in
484 the ionosphere 1. Multistream approach of the transport equations." Journal of
485 Geophysics Research 102 (September): 22261–72.
486 <https://doi.org/10.1029/97JA01903>.
- 487 Green, A. E. S., and L. R. Peterson. 1968. "Energy loss functions for electrons and
488 protons in planetary gases." J. Geophys. Res. 73 (1): 233.
489 <https://doi.org/10.1029/JA073i001p00233>.
- 490 Gronoff, G., J. Lilensten, C. Simon, O. Witasse, R. Thissen, O. Dutuit, and C. Alcaraz.
491 2007. "Modelling Dications in the Diurnal Ionosphere of Venus." Astronomy and
492 Astrophysics 465 (April): 641–45.
493 <http://adsabs.harvard.edu/abs/2007A%26A...465..641G>.
- 494 Gronoff, G., J. Lilensten, C. Simon, M. Barthélemy, F. Leblanc, and O. Dutuit. 2008.
495 "Modelling the Venusian Airglow." Astronomy and Astrophysics 482 (May):
496 1015–29. <http://adsabs.harvard.edu/abs/2008A%26A...482.1015G>.
- 497 Gronoff, G., J. Lilensten, L. Desorgher, and E. Flückiger. 2009a. "Ionization Processes in
498 the Atmosphere of Titan. I. Ionization in the Whole Atmosphere." Astronomy and
499 Astrophysics 506 (November): 955–64.
500 <http://adsabs.harvard.edu/abs/2009A%26A...506..955G>.
- 501 Gronoff, G., J. Lilensten, and R. Modolo. 2009b. "Ionization Processes in the
502 Atmosphere of Titan. II. Electron Precipitation Along Magnetic Field Lines."
503 Astronomy and Astrophysics 506 (November): 965–70.
504 <http://adsabs.harvard.edu/abs/2009A%26A...506..965G>.
- 505 Gronoff, G., C. Simon Wedlund, C. J. Mertens, and R. J. Lillis. 2012a. "Computing
506 uncertainties in ionosphere-airglow models: I. Electron flux and species
507 production uncertainties for Mars." *Journal of Geophysical Research: Space*
508 *Physics*, 117 (April): 4306, 18 PP., <https://doi.org/10.1029/2011JA016930>.
- 509 Gronoff, Guillaume, Cyril Simon Wedlund, Christopher J. Mertens, Mathieu Barthélemy,
510 Robert J. Lillis, and Olivier Witasse. 2012b. "Computing Uncertainties in
511 Ionosphere-Airglow Models: II. The Martian Airglow." J. Geophys. Res. 117
512 (May): 17 PP. <https://doi.org/201210.1029/2011JA017308>.

513 Gronoff, G., Arras, P., Baraka, S., Bell, J. M., Cessateur, G., Cohen, O., Curry, S. M.,
514 Drake, J. J., Elrod, M., Erwin, J., Garcia-Sage, K., Garraffo, C., Glocer, A.,
515 Heavens, N. G., Lovato, K., Maggiolo, R., Parkinson, C. D., Simon Wedlund, C.,
516 Weimer, D. R., & Moore, W. B. (2020), Atmospheric Escape Processes and
517 Planetary Atmospheric Evolution, *Journal of Geophysical Research (Space*
518 *Physics)*, 125(8), e27639, doi:10.1029/2019JA027639.

519 Kozelov, B. V., and V. E. Ivanov. 1992. "Monte Carlo calculation of proton-hydrogen
520 atom transport in N₂." *Plan. Space Sci.* 40 (11): 1503–11.
521 [https://doi.org/10.1016/0032-0633\(92\)90047-R](https://doi.org/10.1016/0032-0633(92)90047-R).

522 Kusakabe, Toshio, Kensuke Asahina, Jiang P. Gu, Gerhard Hirsch, Robert J. Buenker,
523 Mineo Kimura, Hiroyuki Tawara, and Yohta Nakai. 2000. "Charge-transfer
524 processes in collisions of H⁺ ions with H₂, D₂, CO, and CO₂ molecules in the
525 energy range 0.2-4.0 keV." *Phys. Rev. A* 62 (6): 062714.
526 <https://doi.org/10.1103/PhysRevA.62.062714>.

527 Lilensten, J., P. L. Blelly, W. Kofman, and D. Alcaydé. 1999. "Auroral Ionospheric
528 Conductivities: A Comparison Between Experiment and Modeling, and
529 Theoretical F10.7-Dependent Model for EISCAT and ESR." *Ann. Geophys.* 14
530 (12): 1297–1304. <https://doi.org/10.1007/s00585-996-1297-7>.

531 Lummerzheim, D., and J. Lilensten. 1994. "Electron Transport and Energy Degradation
532 in the Ionosphere: Evaluation of the Numerical Solution, Comparison with
533 Laboratory Experiments and Auroral Observations." *Annales Geophysicae* 12
534 (November): 1039–51. <http://adsabs.harvard.edu/abs/1994AnGeo..12.1039L>.

535 McNeal, R. J. 1970. "Production of Positive Ions and Electrons in Collisions of 1-25-keV
536 Protons and Hydrogen Atoms with CO, CO₂, CH₄, and NH₃." *J. Chem. Phys.* 53
537 (11): 4308–13. <https://doi.org/10.1063/1.1673938>.

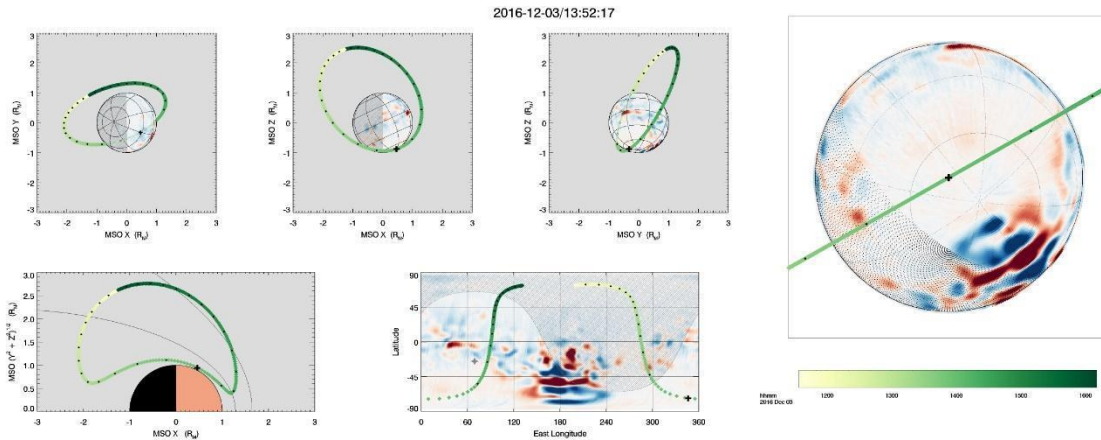
538 Nakai, Y., T. Shirai, T. Tabata, and R. Ito. 1987. "Cross Sections for Charge Transfer of
539 Hydrogen Atoms and Ions Colliding with Gaseous Atoms and Molecules."
540 *Atomic Data and Nuclear Data Tables* 37 (January): 69.
541 [https://doi.org/10.1016/0092-640X\(87\)90005-2](https://doi.org/10.1016/0092-640X(87)90005-2).

542 Nicholson, William P., Guillaume Gronoff, Jean Lilensten, Alan D. Aylward, and Cyril
543 Simon. 2009. "A Fast Computation of the Secondary Ion Production in the
544 Ionosphere of Mars." *Monthly Notices of the Royal Astronomical Society* 400
545 (November): 369–82. <http://adsabs.harvard.edu/abs/2009MNRAS.400..369N>.

546 Rudd, M. E., T. V. Goffe, R. D. Dubois, L. H. Toburen, and C. A. Ratcliffe. 1983. "Cross
547 sections for ionization of gases by 5-4000-keV protons and for electron capture by
548 5-150-keV protons." *Phys. Rev. A* 28 (6): 3244–57.
549 <https://doi.org/10.1103/PhysRevA.28.3244>.

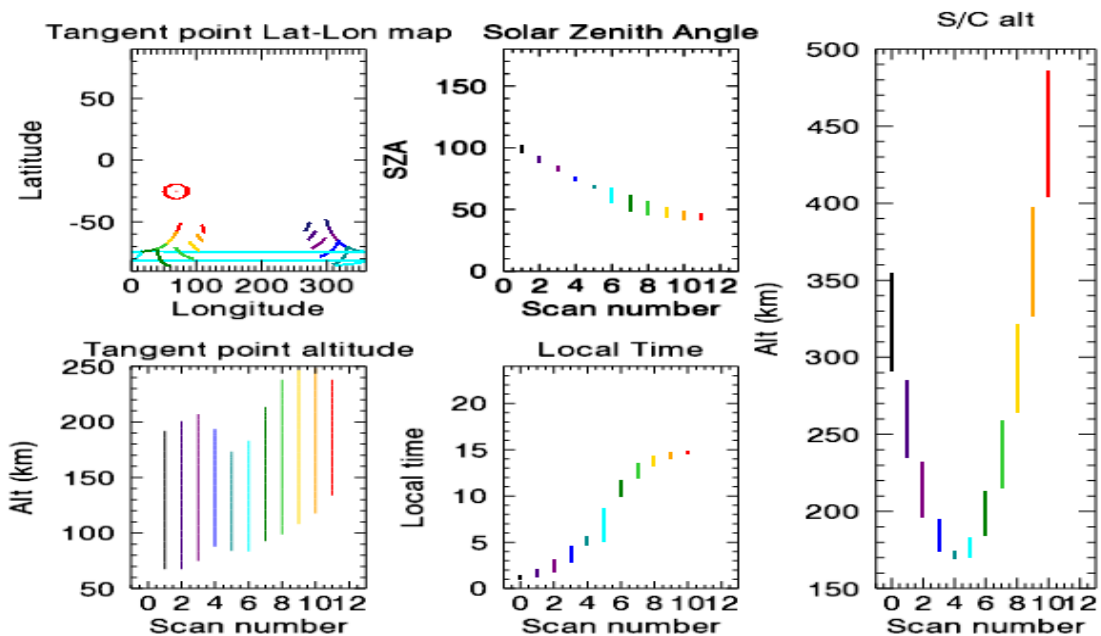
550 Simon, C., J. Lilensten, J. Moen, J. M. Holmes, Y. Ogawa, K. Oksavik, and W. F. Denig.
551 2007. "TRANS4: a new coupled electron/proton transport code - comparison to
552 observations above Svalbard using ESR, DMSP and optical measurements."
553 *Annales Geophysicae* 25 (March): 661–73. [https://doi.org/10.5194/angeo-25-661-](https://doi.org/10.5194/angeo-25-661-2007)
554 [2007](https://doi.org/10.5194/angeo-25-661-2007).

- 555 Simon, C., O. Witasse, F. Leblanc, G. Gronoff, and J.-L. Bertaux. 2009. “Dayglow on
556 Mars: Kinetic Modelling with SPICAM UV Limb Data.” *Planetary and Space*
557 *Science* 57 (July): 1008–21.
558 <http://adsabs.harvard.edu/abs/2009P%26SS...57.1008S>.
- 559 Simon, Cyril. 2006. “Contribution à L’étude Des Entrées d’énergie Solaire Dans
560 L’ionosphère : Ions Doublement Chargés et Transport Cinétique Des Protons -
561 Application à La Terre et à Titan.” PhD thesis, Université Joseph-Fourier -
562 Grenoble I. <http://tel.archives-ouvertes.fr/tel-00109802>.
- 563 Simon Wedlund, C., G. Gronoff, J. Lilensten, H. Ménager, and M. Barthélemy. 2011.
564 “Comprehensive calculation of the energy per ion pair or W values for five major
565 planetary upper atmospheres.” *Annales Geophysicae* 29 (January): 187–95.
566 <https://doi.org/10.5194/angeo-29-187-2011>.
- 567 Smith, K. A., M. D. Duncan, M. W. Geis, and R. D. Rundel. 1976. “Measurement of
568 electron loss cross sections for 0.25- to 5-keV hydrogen atoms in atmospheric
569 gases.” *J. Geophys. Res.* 81 (13): 2231.
570 <https://doi.org/10.1029/JA081i013p02231>.
- 571 Toburen, L. H., M. Y. Nakai, and R. A. Langley. 1968. “Measurement of High-Energy
572 Charge-Transfer Cross Sections for Incident Protons and Atomic Hydrogen in
573 Various Gases.” *Physical Review* 171 (1): 114–22.
574 <https://doi.org/10.1103/PhysRev.171.114>.
- 575 Werbowy, S., and B. Pranszke. 2016. “Charge-exchange processes in collisions of
576 H^+ , H_2^+ , H_3^+ , He^+ , and He_2^+ ions with CO and CO_2 molecules at energies below
577 1000 eV.” *Phys. Rev. A* 93 (2): 022713.
578 <https://doi.org/10.1103/PhysRevA.93.022713>.
- 579 Witasse, O., O. Dutuit, J. Lilensten, R. Thissen, J. Zabka, C. Alcaraz, P.-L. Blelly, *et al.*,
580 2002. “Prediction of a CO_2^+ Layer in the Atmosphere of Mars.” *Geophysical*
581 *Research Letters* 29 (April): 104–1.
582 <http://adsabs.harvard.edu/abs/2002GeoRL..29h.104W>.
- 583 Witasse, O., O. Dutuit, J. Lilensten, R. Thissen, J. Zabka, C. Alcaraz, P.-L. Blelly, *et al.*,
584 2003. “Correction to ‘Prediction of a CO_2^+ Layer in the Atmosphere of Mars’.”
585 *Geophysical Research Letters* 30 (April): 12–11.
586 <http://adsabs.harvard.edu/abs/2003GeoRL..30g..12W>.
587



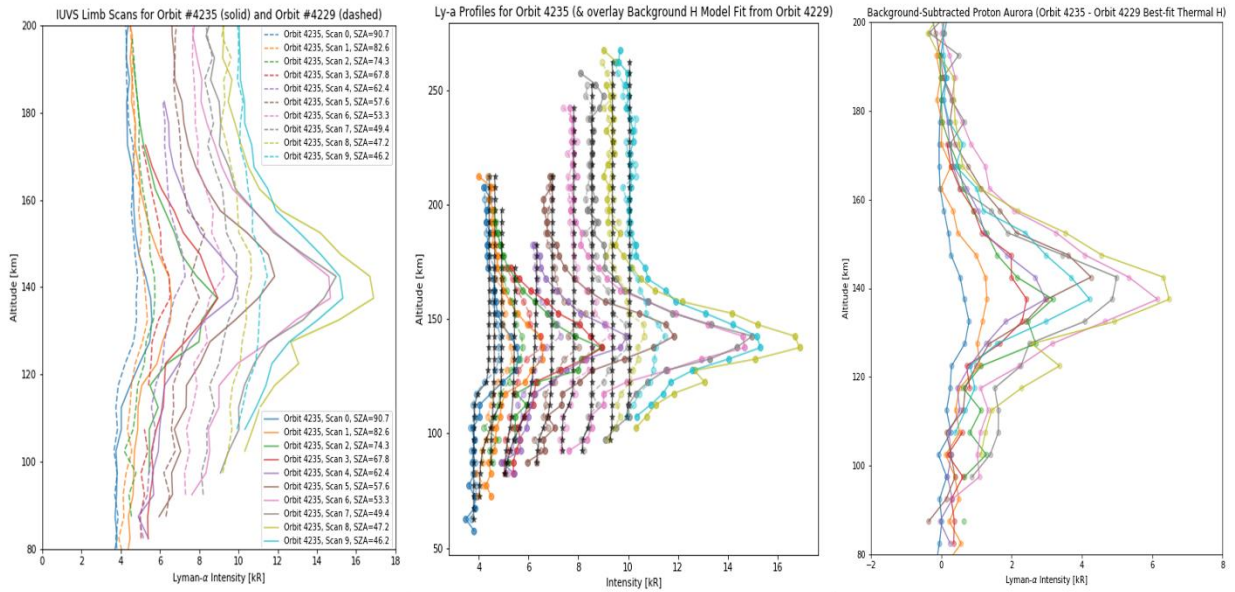
588

589 **Figure S1.** MAVEN spacecraft orbit information showing the locations of the
 590 spacecraft during Orbit 4235. The red/blue colors represent the magnitude and
 591 orientation of the crustal magnetic fields (see MAVEN PDS or Science Data Center
 592 website for more information). Note that the location of the periapsis is in the
 593 southern hemisphere and does not pass over any strong crustal magnetic fields.
 594



595

596 **Figure S2.** MAVEN/IUVS information showing ephemeris data for the IUVS limb
 597 scans during Orbit #4235 periapsis. Note that the location of periapsis is primarily
 598 on the dayside of the planet (with the exception of a few limb scan observations
 599 near the terminator) in the southern hemisphere and does not pass over any strong
 600 crustal magnetic fields. Different limb scans are marked by different colors within
 601 the orbit.
 602

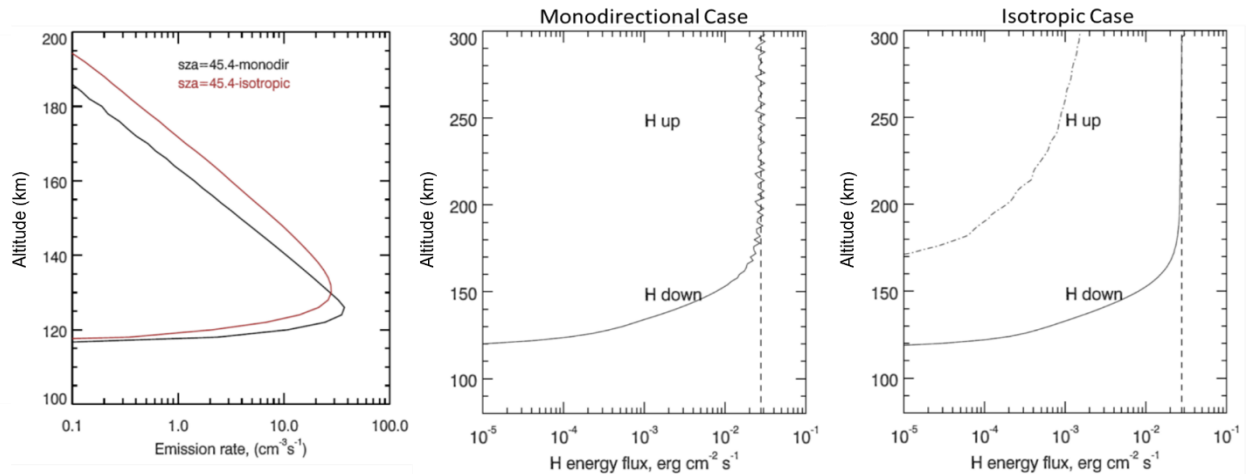


604

605

Figure S3. Altitude-intensity profiles and estimated heuristic thermal H background used for the background subtraction method described in this study. **Left:** IUVS Ly- α profiles for the orbit used in the data-model comparison (#4235), and a nearby orbit with little/less proton aurora activity (#4229) used to create the best-fit heuristic background coronal H profiles for each limb scan; peak profile SZAs for each scan in the two orbits are provided in the legend. **Middle:** Heuristic background thermal H profiles estimated from orbit #4229 (black profiles) overlain on Ly- α profiles for corresponding SZA limb scans in orbit #4235. **Right:** Final background-subtracted profiles that represent the contribution from only H-ENAs in the IUVS proton aurora observation in this orbit (*i.e.*, removing the background contribution from coronal thermal H).

616



618

619

620

621

622

623

624

625

626

627

628

629

630

631

632

633

Figure S4. Example comparison of assuming monodirectional movement of the incident particle population in the atmosphere versus isotropic (simulation results from the Bisikalo/Shematovich *et al.* model). **Left:** Comparison proton aurora profiles using each assumption; **Middle:** Simulated H energy flux in the downward and upward (zero in this case) directions using a monodirectional assumption; **Right:** Simulated H energy flux in the downward and upward directions using an isotropic assumption. The simulated proton aurora profile using the isotropic assumption has a higher peak altitude and smaller VER due to the larger upward H population. The models in this study assume monodirectional particle movement, which could in turn lead to some of the observed discrepancies between the data and the models in Step 2 of the campaign. We note that neither of these two extreme assumptions (*i.e.*, purely monodirectional or purely isotropic incident particle movement) is a probable physical occurrence, and the actual particle precipitation pattern is somewhere between these two limiting cases.

Cross Section (CS) Processes:	Elastic		Charge Exchange/ e ⁻ Capture		e ⁻ Stripping		Ionization		Lyman-α		Lyman-β &/or Lyman-γ		Balmer-α		Excitation of CO ₂		Differential Scattering Cross Sections (DSCS)		
	H-CO ₂	H ⁺ -CO ₂	H-CO ₂	H ⁺ -CO ₂	H-CO ₂	H ⁺ -CO ₂	H-CO ₂	H ⁺ -CO ₂	H-CO ₂	H ⁺ -CO ₂	H-CO ₂	H ⁺ -CO ₂	H-CO ₂	H ⁺ -CO ₂	H-CO ₂	H ⁺ -CO ₂	H-CO ₂	H ⁺ -CO ₂	
Jolitz:	Newman+ 1986 [for H/H ⁺ - N ₂]			Barnett+ 1977	Nakai+ 1987		Van Zyl+, 1978 [for H - O ₂] McNeal, 1970 [rescaling]	Rudd+ 1985	Van Zyl & Neumann [for H - O ₂] Birely & McNeal, 1971 [rescaling]	Avakyan+ 1998 [for H ⁺ - O ₂] Birely & McNeal, 1971 [rescaling]									Newman+ 1986 Noel and Pröls, 1993 [for H/H ⁺ - O ₂]
Kallio:	Newman+ 1986 [for H/H ⁺ - N ₂]			Rees, 1989 [for H ⁺ - O ₂]	Van Zyl+, 1978 [for H - O ₂]		Van Zyl+, 1978 [for H - O ₂]	Rudd+ 1985	Van Zyl & Neumann, 1988 [for H/H ⁺ - O ₂]										Newman+ 1986 Noel and Pröls, 1993 [for H/H ⁺ - O ₂]
Bisikalo/ Shematovich et al.:	Porter+ 1976			Nakai+ 1987 [for H - O ₂ and rescaled]	Nakai+ 1987 [for H - O ₂ and rescaled]		Haider+ 2002 [for H - O ₂ and rescaled]		Haider+ 2002 [for H - O ₂ and rescaled]										Lindsay+ 2005 [for H/H ⁺ - O ₂ and rescaled]
Gronoff et al.:	Kozelov & Ivanov, 1992 [for H/H ⁺ - N ₂]			Kusakabe+ 2000 Avakyan+ 1998	Smith+ 1976 Avakyan+ 1998 [for H - N ₂]		Basu+ 1987 [for H - N ₂] Avakyan+ 1998 [rescaling]	Rudd+ 1983 Avakyan+ 1998	Birely & McNeal, 1972 [rescaled as per Avakyan+ 1998]										Avakyan+ 1998 Basu+ 1987 [Calculated from pitch angle using Rutherford-type collision functions]

Table S1. List of cross sections (CS) that each model in this study may include. The five overlapping CS processes of each modeling team are shown in green, along with relevant references for those CS processes and Differential Scattering Cross Sections (DSCS). Bins marked with an “X” represent additional CS processes that can be included in models.